Design and Modeling of a Solar Reactor for Thermochemical Carbon Dioxide Capture

A Dissertation
SUBMITTED TO THE FACULTY OF THE
UNIVERSITY OF MINNESOTA
BY

Leanne Cynthia Reich

IN PARTIAL FULFILLMENT OF THE REQUIREMENTS
FOR THE DEGREE OF
DOCTOR OF PHILOSOPHY

Dr. Wojciech Lipiński and Dr. Terrence Simon, Advisers

June 2015

ACKNOWLEDGEMENTS

I'd like to thank the following people for their contributions to this work:

- My advisers, Dr. Wojciech Lipiński and Dr. Terry Simon, for their inspiration and guidance throughout the course of my graduate work.
- My colleagues in the Heat Transfer and Solar Energy laboratories at the University of Minnesota for helpful discussions and suggestions.
- Dr. Brandon Hathaway and Dr. Roman Bader for their assistance in setting up and debugging the radiation modeling code.
- The Solar Thermal Group at The Australian National University in Canberra for making me feel welcome and at home on the other side of the world.
- Luke Melmoth and Rob Gresham for taking the reactor concept and making it a practical reality.
- All of the administrative staff for your assistance, especially John Gardner and Kylee Robinson.

I am grateful for the financial support of the U.S. National Science Foundation and the University of Minnesota Initiative for Renewable Energy and the Environment. This work was carried out in part using computing resources from the University of Minnesota Supercomputing Institute.

DEDICATION

To Mom, Dad, Charles, Grandma Nancy, Grandpa Bill, Grandma Sue, Grandpa Dave, and the rest of my family for never ending support and encouragement.

To Dr. Robert Palumbo for starting my engineering toolbox and teaching me to do good research.

To the ladies of the women in graduate school support group, who taught me the importance of nibbles, self-care, and cutting myself some slack.

To my graduate student friends, especially Katie Krueger, Matt McCuen, David Osterhouse, Karl Stathakis, Katie Goetz, and Jessica Williamson, for listening and understanding in a way that no one outside graduate school could.

To the members of Gethsemane Lutheran Church in Hopkins, MN, for creating a welcoming community of faith.

To the St. Louis Park Community Band for being fantastic musicians and making me look forward to playing at rehearsal each week.

And finally, to Wade, for always being there to listen to me gush on the good days and gripe on the bad ones. I love you.

ABSTRACT

The development and design of a 1 kW research-scale solar-driven reactor to study the calcium oxide-based carbonation–calcination cycle for carbon dioxide capture is presented. Thermodynamic analyses are used to identify appropriate reaction conditions and evaluate the usefulness of gas and solid heat recovery. A numerical heat and mass transfer model is developed, first to support the design of the reactor and then to predict the solar-to-chemical conversion efficiency. The model solves the mass, momentum, and energy conservation equations and includes the effects of radiative heat transfer and chemistry. The final reactor design consists of a beam-up oriented inner cavity surrounded by a packed bed of reacting particles. It is intended to be easy to assemble and modify, allowing for future design improvements.

TABLE OF CONTENTS

LIST OF TABLES

LIST OF FIGURES

NOMENCLATURE

A	area, m^2
C	solar flux concentration ratio
C	chemical concentration, mol m^{-3}
C_f	Forchheimer coefficient, m^{-1}
$\overline{c_p}$	specific heat at constant pressure, kJ mol^{-1} K^{-1}
D	diameter, m
E	energy, J
E_a	activation energy, kJ mol^{-1}
F_{i-j}	geometric view factor
$f_{v,s}$	solid volume fraction
G_0	direct solar irradiation, W
$\overline{g}$	molar Gibbs function, J mol^{-1}
H	cavity height, m
H_o	incident flux, W m^{-2}
h	enthalpy, kJ
$\overline{h}$	specific enthalpy, kJ mol^{-1}
$\Delta\overline{h}^o_{298K}$	standard molar enthalpy of reaction, kJ mol^{-1}
$\overline{HHV}$	molar higher heating value of fuel, kJ mol^{-1}
I	radiative intensity, W m^{-2} sr^{-1}
$\hat{\mathbf{i}}$	unit vector in r direction
$\hat{\mathbf{j}}$	unit vector in ϕ direction
$\hat{\mathbf{k}}$	unit vector in z direction
k	thermal conductivity, W m^{-1} K^{-1}
k	rate constant, various units
K	permeability, m^2
M	mass, kg
$\overline{M}$	molar mass, kg $kmol^{-1}$
m	complex index of refraction, $m = n - ik$
N	number of rays
n	refractive index
n	amount of substance, mol
n_r	number of radial divisions
n_θ	number of angular divisions
n_z	number of axial divisions

$\hat{\mathbf{n}}$	normal unit vector
p	pressure, kPa
$\overline{Q}$	molar specific heat, kJ $\text{mol}^{-1}_{\text{CO}_2,\text{captured}}$
q	heat rate, W
q''	heat flux, W m^{-2}
$\overline{R}$	universal gas constant, J mol^{-1} K^{-1}
$\Re$	random number
r	radius, m
$\vec{\mathbf{r}}$	ray origin vector
$\dot{r}$	reaction rate, mol m^{-3} s^{-1}
S	specific surface area, m^2 m^{-3}
$\vec{\mathbf{S}}$	source term
$\vec{\mathbf{s}}$	direction vector
T	temperature, K
t	time, s
$\hat{\mathbf{t}}$	tangential unit vector
u	velocity component, m s^{-1}
$\hat{\mathbf{u}}$	ray direction unit vector
V_r	reactor volume, m^3
v	fluid speed, m s^{-1}
$\vec{\mathbf{v}}$	velocity vector, m s^{-1}
$\overline{W}$	molar specific work, kJ $\text{mol}^{-1}_{\text{CO}_2}$
X	reaction extent
x	value
$\bar{x}$	molar fraction
z	axial location, m

Abbreviations

CFD	computational fluid dynamics
MC	Monte Carlo
NRM	net radiation method
UDF	user defined function
UDM	user defined memory

Greek

β	extinction coefficient
γ	coefficient defined by Eq. (2.3a)
ε	fraction heat recovery
ε	emissivity
η	solar to chemical conversion efficiency

η_{abs}	solar absorption efficiency
θ	elevation angle, rad
κ	absorption coefficient
λ	wavelength, μm
μ	viscosity, Pa s
ξ	coefficient defined by Eq. (2.3b)
ρ	density, kg m^{-3}
σ	Stefan–Boltzmann constant, σ = 5.6704×10^{-8} W m^{-2} K^{-4}
σ_s	scattering coefficient
τ	optical thickness
$\boldsymbol{\tau}$	shear stress, Pa
Φ	scattering phase function
ϕ	azimuth angle, rad
ψ	azimuth angle, rad
Ω	solid angle, sr

Subscripts

abs	absorbed
ap	aperture
av	average
c	combustion
calc	calcination
carb	carbonation
cav	cavity
dg	CO_2 depleted gas
eff	effective
eq	equilibrium
f	fluid
fc	fuel cell
g	gas
gs	gas–solid
H	hot
ig	input gas
i,j,k	surface indices
int	intersection
min	minimum
n	normal
p	particle
p	products
r	reactants
r	radial
rad	radiation

rerad	reradiation	z	axial
s	solid	0	initial
t	tangential	1…9	at positions indicated in Fig. 2.1
tot	total	∞	ambient

CHAPTER 1: INTRODUCTION

1.1 Motivation

Global climate change caused by greenhouse gas emissions is a growing problem in the modern world. In 2008, 98% of carbon dioxide emissions in the United States and 93% worldwide were energy related [1,2]. Carbon dioxide makes up 80% of all greenhouse gas emissions in the United States and 77% worldwide. Worldwide energy use continues to grow at a rate of about 1.6% per year, and 87% of that energy comes from fossil fuel sources [3,4]. If the world continues to rely on fossil fuels for energy, carbon dioxide capture systems will be necessary in order to reduce the effect of climate change due to greenhouse gas emissions.

Hydrocarbon fuels are projected to continue to dominate the transportation sector for the foreseeable future. Their high energy density, ease of handling, and well developed distribution infrastructure contributes to this dominance, but fossil fuel resources will eventually be depleted or become to cost prohibitive to extract. However, production of synthetic hydrocarbon fuels from a mixture of hydrogen and carbon monoxide called synthesis gas is an option [5]. There are a number of ways to produce synthesis gas, including metal oxide redox cycles. The production of the carbon monoxide component requires a concentrated stream of carbon dioxide as a reactant. A system for carbon dioxide capture would be able to supply such a stream, resulting in a closed carbon cycle where CO_2 is produced through combustion, captured, and reused to produce additional fuel.

Many carbon dioxide capture technologies have been investigated over the years, including pre-combustion capture, post combustion capture, oxycombustion, and capture from industrial processes [6]. Methods used by capture technologies include physical or chemical absorption, adsorption, membrane separation, and cryogenic separation [7]. One chemical absorption approach involves calcium oxide carbonation combined with calcium carbonate calcination:

Carbonation step (exothermic): $\mathrm{CaO+CO_2 \rightarrow CaCO_3}$, $\Delta h^0_{298K} = -178 \text{ kJ mol}^{-1}$ (1.1a)

Calcination step (endothermic): $\mathrm{CaCO_3 \rightarrow CaO+CO_2}$, $\Delta h^0_{298K} = 178 \text{ kJ mol}^{-1}$ (1.1b)

This cycle is advantageous because it operates at low pressures, can capture more CO_2 per unit mass of sorbent than other processes, and uses CaO as a low cost sorbent that is produced from natural limestone and dolomite [8,9].

Reaction (1.1b) requires a high temperature process heat source, proceeding at temperatures above 1150 K. Since this temperature is typically achieved via combustion of fossil fuels, integrating CaO based CO_2 capture with a power plant reduces the efficiency. An alternative to combustion that could be used to drive this process is concentrated solar energy. With this method, additional CO_2 is not produced elsewhere because the power output of the plant remains the same. Concentrated solar radiation has been used to provide high temperature process heat for many thermochemical processes and can potentially run continuously if connected to thermal storage [10,11]. In addition, this type of two-step process can be used for solar thermochemical energy storage if the

energy released in the carbonation reaction is harnessed to produce steam for electricity generation [12,13].

1.2 Literature Review

1.2.1 Thermodynamics

Carbon dioxide capture using a CaO based cycle was first proposed by Shimizu et al. [14]. A pair of conceptual fluidized beds connected by solid transport pipes and attached to a 1000 MW air-fired coal power plant was studied. The carbonation temperature was 873 K and the calcination temperature was 1223 K. Heat was recovered from the exothermic carbonation reaction and the cooling stream of CO_2 using a secondary steam cycle. Use of heat recovery boosted the plant efficiency to 33.4% compared to 32% for an oxygen-fired coal plant.

The heat requirement in the calciner of a system capturing CO_2 with CaO was studied by Rodriguez et al. [15]. The effects of CaO conversion, ratio of sorbent flow between the calciner and carbonator to CO_2 flow entering the carbonator, and coal composition on the heat required for calcination as a percentage of the heat input to the power plant were investigated. For a case with no makeup flow of sorbent at a residual CaO conversion of 0.075 and no sulfur present in the fuel, the heat requirement in the calciner was 36.9% of the heat required for the power plant. Using the data from [15] and assuming a capture rate of 1 mol CO_2 per second, this translates into an energy requirement of about 3.9 MJ per mol of CO_2 captured.

Martinez et al. examined the effects of adding solid heat recovery to the cycle by simulating four different solid heat exchange configurations [16]. Indirect solid heat exchange between hot CaO and cool $CaCO_3$ was the most efficient option, increasing thermal efficiency by up to 2% compared to a case with no solid heat recovery. A solid heat exchange system with a mixing seal valve showed no improvement compared to the base case. A system with a heat recovery fluidized bed preheating $CaCO_3$ with hot CO_2 increased thermal efficiency by up to 1.4%.

Thermodynamic analysis of a solar-driven carbonation–calcination cycle for capture of atmospheric CO_2 was conducted by Nikulshina et al. [17]. The carbonation temperature was 500 K and the calcination temperature was 1500 K with an inlet gas CO_2 concentration of 500 ppm. The reaction studied had an added step of reacting the CaO with water in a slaker at 353 K to form $Ca(OH)_2$ in order to improve the kinetics of the carbonation reaction as $Ca(OH)_2$ carbonation avoids the diffusion limitation encountered in CaO carbonation [18]. The total energy required for the cycle without the use of heat exchangers was 12.1 MJ per mole of captured CO_2 and 2.5 MJ per mole of captured CO_2 with the use of two heat exchangers, one to preheat the input gas to the carbonator with hot CO_2 depleted gas, and one to preheat $CaCO_3$ entering the calciner with hot CO_2.

1.2.2 Chemical Kinetics

The kinetics of the calcination reaction have been extensively studied. Borgwardt studied the kinetics of the calcination of two different limestones with particle diameters ranging from 1 to 90 μm using a differential reactor [19]. At 850°C, the reaction was

linearly dependent on $CaCO_3$ surface area with a rate constant of 1.6×10^{-6} mol cm^{-2} s^{-1}. The activation energy was 205 kJ mol^{-1}. Dennis and Hayhurst found the rate constant to be 1.0×10^{-6} mol cm^{-2} s^{-1} and the activation energy to be 169 kJ mol^{-1} at the same temperature, but noted that the rate was a function of both CO_2 partial pressure and total pressure [20]. They also found that the reaction was chemically controlled and that increasing the total pressure increased the reaction time regardless of CO_2 partial pressure. Escardino et al. summarized the results of several studies from 1930–1974, noting that the reported reaction order varied from 0 to 1 and the reported activation energy varied from 147 to 397 kJ mol^{-1} [21]. Their own study obtained an activation energy of 175 kJ mol^{-1} and a reaction order of 1/3. Garcia-Labiano et al. studied the calcination reaction using several sources of limestone [22]. They found that the pre-exponential factor of the Arrhenius equation ranged from 29.5 to 6.7×10^{6} mol m^{-2} s^{-1} and that the activation energy ranged from 114 to 166 kJ mol^{-1} depending on the sorbent source. Acharya et al. studied the calcination reaction in atmospheres of N_2, steam, and CO_2 [23]. They found that the pre-exponential factor ranged from 2.12 to 4.82×10^{10} s^{-1} and that activation energy ranged from 180 to 257 kJ mol^{-1}. The N_2 atmosphere had the highest pre-exponential factor and activation energy and the CO_2 atmosphere had the lowest.

The kinetics of the carbonation reaction have also been widely studied. The reaction is generally considered to be chemically controlled initially and switches to a diffusion controlled regime due to formation of a $CaCO_3$ product layer. Bhatia and Perlmutter

found the reaction rate constant to be an average of 0.0595 cm^4 $gmol^{-1}$ s^{-1} for temperatures ranging from 550 to 725°C and gas atmospheres containing 2 to 10% CO_2 [24]. Shimizu et al. found the reaction rate to be linearly dependent on CO_2 concentration, but the maximum conversion decreased as the CaO was cycled [14]. The reaction rate constant was unaffected by cycling and had an average value of 25 m^3 $kmol^{-1}$ s^{-1} for reaction atmospheres containing 5 to 15% CO_2. Fang et al. found the rate constant to be 2.1 x 10^{-3} m^3 mol^{-1} s^{-1} for the chemically controlled initial reaction and 2.5 x 10^{-3} m^3 mol^{-1} s^{-1} for the diffusion controlled regime for a reaction atmosphere of 20% CO_2 [25].

A summary of the rate equations for both the calcination and carbonation reactions from various studies is shown in Table 1.1.

Table 1.1: Summary of rate equations for calcination and carbonation

	Rate equation	Rate constant	Ref.
Calcination	$\ln(1-X) = -k_s a t$	$2.5\text{x}10^{-8}$ mol cm^{-2} s^{-1}	[19]
	$r_c = \bar{k}(p^*_{CO_2} - p_{CO_2})$	$\bar{k}$ = 0.207 mol bar^{-1} m^{-2} s^{-1}	[20]
	$\frac{dX}{dt} = k\frac{(1-X)(p_{eq}-p_{CO_2})}{p_{eq}},\ k = k_0\exp(\frac{-E_a}{RT})$	$k_0=2.12\text{x}10^6$–$4.82\text{x}10^{10}$ s^{-1}, E_a=180.56–257.78 kJ mol^{-1}	[23]
	$\frac{dX}{dt} = k(1-X)^m,\ k = k_0\exp(\frac{-E_a}{RT})$	$k_0=6.45\text{x}10^5$ s^{-1}, E_a=187.3 kJ mol^{-1}	[26]
	$\frac{dX}{dt} = k(1-X)^{2/3}(C_{CO_2} - C_{eq,CO_2}),$ $k = k_0\exp\left(\frac{-E_a}{RT}\right)$	$k_0=2.3797\text{x}10^4$ m^3 mol^{-1} s^{-1}, E_a=150 kJ mol^{-1}	[25]
Carbonation	$\frac{dX}{dt} = kCX_{\max}\exp(-kCt)$	k=25 m^3 mol^{-1} s^{-1}	[14]
	$\frac{1}{\psi}[\sqrt{1-\psi\ln(1-X)}-1] = \frac{k_s a_o (C-C_{eq})t}{2(1-\varepsilon_o)},$ $\frac{1}{\psi}[\sqrt{1-\psi\ln(1-X)}-1] = \frac{a_o}{(1-\varepsilon_o)}\sqrt{\frac{bMC_s t}{2a\rho Z}}$	k_s=0.0595 cm^4 mol^{-1} s^{-1}	[24]
	$\frac{dX}{dt} = k_c(1-\frac{X}{X_{\max}})^m(C_{CO_2} - C_{eq,CO_2})$	Kinetically controlled: k_c=0.0021 m^3 mol^{-1} s^{-1}, m=2/3 Diffusion controlled: k_c=0.0025 m^3 mol^{-1} s^{-1}, m=4/3	[25]
	$\frac{dX}{dt} = kS(1-X)^{2/3}(p_{CO_2} - p_{eq,CO_2}),$ $k = k_0\exp\left(\frac{-E_a}{RT}\right)$	$k_0=1.67\text{x}10^{-4}$ mol m^{-2} s^{-1} kPa, $E_a=2.9\text{x}10^4$ J mol^{-1}, $S=2.8006\text{x}10^7$ m^2 m^{-3}	[27]
	$\frac{dX}{dt} = k\left(1-\frac{X}{X_u}\right)^2, k = k_0\exp\left(\frac{-E_a}{RT}\right)$	$k_0=1.03\text{x}10^4$ min^{-1}, E_a=72.2 kJ mol^{-1}, X_u=0.75	[28]

1.2.3 Reaction Modeling

In addition to chemical kinetics, heat and mass transfer to and from the reacting particles also influence reaction rates and reaction conversion. Several numerical models in the literature have investigated these effects at the level of a single particle.

The effect of particle size, reaction rate, internal radiative heat transfer, permeability, incident solar flux, and partial pressure of CO_2 on reaction rate, temperature, and overall reaction extent in a single particle undergoing calcination were studied by Yue and Lipiński [29]. A reaction front that proceeded from the surface of the particle to the center as the reaction progressed was observed. The temperature profiles in the particle demonstrated a similar time progression, with temperatures increasing until the onset of reaction, remaining constant until reaction completion, and then increasing again. Particle size and incident solar flux had the largest effect on the overall reaction extent at a given time. The authors observed a critical particle radius below which the conversion time stopped decreasing as a result of convective losses at the particle surface preventing the center of the particle from reaching the needed temperatures for reaction. Increasing the incident solar flux increased the rate of conversion. Overall, heat transfer limitations were more important than chemical kinetics or mass transfer limitations.

Stendardo and Foscolo developed a numerical model of the carbonation of a calcined dolomite particle that included the effects of diffusion through the product layer [30]. The model was able to adequately predict incomplete carbonation conversion due to this diffusion limitation. The effect of cycling on the final carbonation conversion was also

predicted well by the model. Particles with larger grain sizes demonstrated better overall reaction conversion, as did those with higher levels of MgO.

1.2.4 Reactor Design

The first portion of this section discusses experimental studies of combustion-based CaO carbonation–calcination CO_2 capture processes. The majority of experimental work to date has been in combustion-based processes. The second portion discusses solar-based processes for both calcination and CO_2 capture. The full solar-based cycle has not been as extensively studied, so calcination experiments in practical reactors have been presented in order to compare performance parameters.

A batch mode fluidized bed for the CaO carbonation–calcination cycle was studied at the pilot scale by Abanades et al. [31]. The fluidized bed was shown to be effective for CO_2 capture at a temperature near 650°C. The carbonation reaction was fast enough at atmospheric pressure to completely remove CO_2 from the input gas at a bed height of 0.25 m. The reactivity of the CaO decreased with an increased number of cycles, although the rate of decay and the residual conversion depended on the type of limestone used. Havelock limestone behaved similarly to limestone in other studies and performed better than Cadomin limestone.

A 75 kW pilot scale dual fluidized bed setup was investigated by Lu et al. [32]. It was the first to feature a continuous cycle utilizing two beds rather than a batch cycle where carbonation and calcination occurred in the same location. Cyclones collected particles from the top of the carbonator and cycled them to the calciner and vice versa. The solids

flow was controlled by solenoid valves. The nominal CO_2 concentration entering the carbonator was 15%. Heat was supplied to the calciner by electric heaters or by burning biomass or coal. The calcination temperature ranged from 850 to 950°C and the carbonation temperature ranged from 580 to 720°C. During the first several cycles CO_2 capture efficiency, defined as the percentage of CO_2 removed from the inlet gas, was greater than 90%, but began to decrease after 10 cycles. After 25 cycles, the CO_2 capture efficiency was around 70%. Increasing the carbonation temperature improved the efficiency in later cycles. The authors speculated that this is due to particle sintering and pore plugging blocking the ability for CO_2 to reach deep pores after cycling of the sorbent.

Several other laboratory scale dual fluidized bed setups have been investigated, and three were summarized by Rodriguez et al. [33]. The facilities were 10–75 kW dual fluidized beds operating in several regimes of fluidization located in Spain, Germany, and Canada. Carbonation temperatures ranged from 600–700°C and calcination temperatures ranged from 800–900°C. Two of the facilities operated continuously while the other was semi-continuous. The semi-continuous setup allowed for the effect of cycling to be observed at the expense of achieving steady state, while the continuous setups contained a mixture of particles with different histories but could achieve steady state operation. Each facility used different fuel and limestone sources, but all achieved CO_2 capture efficiencies above 70%, demonstrating that CO_2 capture using fluidized beds is industrially viable for a wide range of conditions.

Flamant et al. first studied the solar driven decomposition of $CaCO_3$ in 1980 [34]. A quartz tube reactor containing a fluidized bed of $CaCO_3$ demonstrated 100% calcination conversion and negligible thermal gradients between 600 and 1300°C. A rotary kiln reactor was also investigated, but only achieved 60% calcination conversion and had significant thermal gradients along its length. The quartz tube setup had an energy requirement of 9 kWh per kg of CaO while the rotary kiln needed 63 kWh per kg of CaO. However, the rotary kiln was a better solar absorber. The major losses in the quartz tube were radiative, which could be improved by increasing the absorptivity of the fluidized bed by adding a secondary material or adding reflectors around the tube, and the major losses in the kiln were due to conduction through the outer walls, which could be improved with increasing insulation or reduction of the water cooling present.

Steinfeld et al. demonstrated a 3 kW solar cyclone reactor open to the atmosphere for decomposition of $CaCO_3$ [35]. This reactor had the advantage of being windowless, as the quartz windows typically used in solar reactors are expensive and fragile. The total absorption efficiency of the reactor was 43%, defined as the ratio of energy absorbed by the reactor to energy entering the aperture. The authors also calculated kinetic parameters, obtaining values of 7.24×10^4 s^{-1} for the pre-exponential factor and 156.8 kJ mol^{-1} for the activation energy.

A 10 kW solar rotary kiln reactor for lime production was developed by Meier et al. [36]. It achieved a solar to chemical conversion efficiency that averaged 13% with a maximum near 20% and had an average CaO production rate of 0.33 g s^{-1}. The authors

noted that the efficiency can be improved by reducing convection losses from the open aperture, improving insulation, and recovering heat from the hot reaction products. The design was later improved by adding absorber tubes to the rotating cavity, through which limestone particles passed and were indirectly heated [37]. The reactor produced up to 98% pure CaO at rates up to 1.07 g s^{-1} and achieved solar to chemical conversion efficiencies of up to 34%. Losses were mainly due to reradiation, but about 14% of the input solar energy was lost to conduction through the reactor walls and 15% was lost due to other causes, including convection losses from the aperture.

A solar-driven carbonation–calcination cycle for capturing CO_2 was demonstrated at the laboratory scale by Nikulshina et al. [38]. The reactor was a quartz tube with a fluidized bed of CaO or $CaCO_3$ particles mixed with SiO_2 particles placed in the focus of a high flux solar simulator. The carbonation inlet gas was air containing 500 ppm CO_2 and 17% water vapor at a temperature of 365–400°C. The calcination inlet gas was argon at temperatures between 800 and 875°C. Five carbonation–calcination cycles were performed and no degeneration of the sorbent was observed, which the authors attributed to the addition of water vapor. During carbonation, less than 1 ppm CO_2 was observed in the exit gas for 1800 seconds, after which the reaction slowed due to a diffusion layer of $CaCO_3$ forming on the outside of the particles. They reported fast attainment of a uniform temperature in the reactor due to the fluidized bed design. A later study investigated the effect of water vapor concentration and carbonation temperature [39]. The authors found that the presence of steam improved the surface kinetics but the concentration of steam

had little effect on the final extent of reaction. Increasing the reaction temperature increased the fraction of CaO conversion at 2500 seconds from 0.28 at 300°C to 0.48 at 380°C.

To date, researchers have demonstrated that CO_2 capture via the CaO carbonation–calcination cycle is a feasible method. It has been shown that fluidized beds are suitable for the process because they have the potential to improve heat and mass transfer in the reactor and can be scaled up as needed. However, while there has been a large body of research conducted regarding CO_2 capture with CaO using fossil energy, using concentrated solar energy to drive the cycle is a relatively new concept. In addition, all of the solar powered reactors described above either only perform calcination or are a simple quartz tube.

1.3 Research Objectives

The primary objective of this research is to develop a 1 kW_{th} laboratory scale solar-driven reactor to study the CaO-based CO_2 capture process using a combination of analytical and numerical analysis. The work presented in this thesis focuses on 3 main tasks: thermodynamic analysis, solar reactor design, and thermal transport modeling. The thermodynamic analysis, presented in Chapter 2, examines the effect of reaction temperatures, CO_2 concentration in the input gas to the carbonator, and gas and solid heat recovery effectiveness on the total heat required for the process, providing a baseline guide to selecting operating conditions for the reactor. From these conditions, a reactor concept is selected from a number of ideas described in Chapter 3. In Chapter 4, a steady

state thermal transport model is used to evaluate a range of potential reactor sizes and select the most suitable size in terms of heat transfer to the reaction zone, temperature uniformity, and pressure drop. The thermal transport model is also used to support and evaluate the mechanical design of the reactor as described in Chapter 5. Finally, in Chapter 6, a transient thermal transport model including the effects of the calcination reaction on heat and mass transfer is used to predict the solar-to-chemical conversion efficiency of the reactor.

CHAPTER 2: THERMODYNAMIC ANALYSIS[1]

2.1 Introduction

Prior studies of the carbonation–calcination process are mainly focused on kinetics and experimental methods rather than thermodynamics. Those that have looked at the thermodynamics did not address the effect of varying the calcination temperature or amount of heat recovery, nor did they account for the solar absorption efficiency [16,17]. In this chapter a thermodynamic analysis to examine the effects of carbon dioxide concentration, gas and solid phase heat recovery, and carbonation and calcination reaction temperatures on the total energy required for an ideal solar-driven and continuously operated CO_2 capture cycle based on the CaO carbonation–calcination process is described. The results are used to set design objectives for the reactor, focusing on minimizing the heat required for the cycle.

2.2 Problem Statement

The model system is shown in Fig. 2.1. The input gas with CO_2 molar fraction $\bar{x}_{0,CO_2}$ enters the system at temperature T_0. The gas is preheated with heat recovered from three sources: CO_2-depleted gas exiting the carbonator at T_{carb} to T_1, CO_2 at T_7 to T_2, and the

---

[1] Material in this chapter has been published in: L. Matthews and W. Lipiński. Thermodynamic analysis of solar thermochemical CO_2 capture via carbonation/calcination cycle with heat recovery. *Energy* 45:900–907, 2012 [77].

exothermic carbonation reaction to T_3 before entering the carbonator. The CO_2 in the input gas reacts with CaO in the carbonator, forming $CaCO_3$. CO_2-depleted gas exits the carbonator and the $CaCO_3$ is cycled to the calciner, which is a perfectly insulated solar receiver. The $CaCO_3$ is preheated on the way to the calciner to T_4 and T_6 by hot CaO and CO_2 exiting the calciner, respectively. Once it enters the calciner, the $CaCO_3$ is heated by concentrated solar radiation to T_{calc}. The solar radiation also provides process heat for the calcination reaction, where $CaCO_3$ dissociates back into CaO and CO_2. The produced CaO is cycled back to the carbonator and the CO_2 exits the system after being used for preheating.

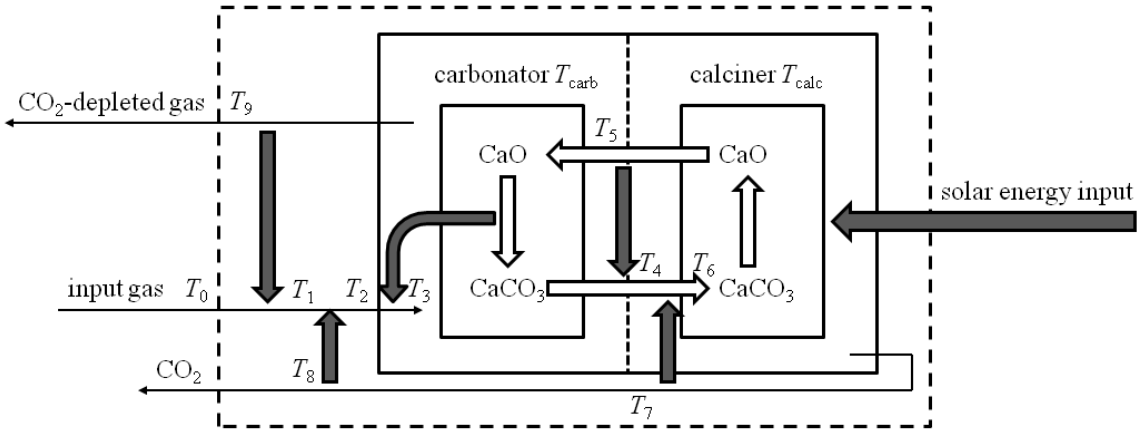

Figure 2.1: Two-step carbonation–calcination cycle for CO_2 capture. Thin black arrows indicate gas flow, large white arrows indicate solid mass flow, and large gray arrows indicate heat flow.

Typical concentrations and pressures of exhaust gases leaving various types of power plants and other CO_2-producing processes are illustrated in Table 2.1 [6]. Depending on heat recovery, the exit temperature of the stack varies between 373 and 473 K. Typical CO_2 concentrations in the exhaust gas are between 3 and 15%. For this reason, the

calculations described in this chapter are conducted for CO_2 molar fractions between 0.0003 (atmospheric concentration) and 0.15.

Table 2.1: Typical exit gas conditions for several CO_2 producing processes [6]

Source	CO_2 Concentration (%)	Pressure (MPa)
Natural gas fired boiler	7–10	0.1
Gas turbine	3–4	0.1
Oil fired boiler	11–13	0.1
Coal fired boiler	12–14	0.1
IGCC after combustion	12–14	0.1
IGCC after gasification	8–20	2–7
Oil refinery/petrochemical plant fired heaters	8	0.1
Blast furnace gas		
-Before combustion	20	0.2–0.3
-After combustion	27	0.1
Cement kiln off-gas	14–33	0.1

Table 2.2 lists the baseline parameters used for the study. For CO_2 molar fractions less than 0.01, the input gas is composed of CO_2, O_2, and N_2 to simulate atmospheric air. For molar fractions higher than 0.01, the input gas contains CO_2 and N_2 to simulate combustion gases after desulfurization. Any water vapor present in the flue gas is assumed to be condensed out prior to the process. The amount of CaO in the carbonator is matched to the molar fraction of CO_2 in the input gas to achieve complete carbonation with respect to the solid phase. At equilibrium, the total amount of CO_2 captured is related to $\bar{x}_{0,CO_2} - \bar{x}^*_{CO_2}$, where $\bar{x}_{0,CO_2}$ and $\bar{x}^*_{CO_2}$ are the molar fraction of CO_2 in the input gas and the equilibrium molar fraction of CO_2, respectively. The total number of moles of CaO needed to fully react with the incoming CO_2 is

$$n_{CaO} = (\bar{x}_{0,CO_2} - \bar{x}^*_{CO_2}) n_g \tag{2.1}$$

where n_g is the total number of moles of input gas. $\bar{x}^*_{CO_2}$ for the calcination reaction is always greater than 1 for the temperature ranges studied, and so the calcination reaction always goes to completion. Thus, the number of moles of CaO in the carbonator is equal to the number of moles of $CaCO_3$ in the calciner and the number of moles of CO_2 released in calcination. The CO_2-depleted gas exiting the carbonator contains $n_{0,CO_2} - n_{CaO}$ moles of CO_2 and the original amounts of N_2 and O_2.

Table 2.2: Baseline calculation parameters for the thermodynamic analysis

Parameter	Value
T_{carb}	673 K
T_{calc}	1273 K
T_0	298 K
$\bar{x}_{0,CO_2}$	0.1
p_{tot}	100 kPa
$p_{CO_2,calc}$	100 kPa CO_2
C	1000
G_0	1 kW m^{-2}

2.3 Analysis

An energy balance is performed on the cycle of Fig. 2.1 to determine the influence of selected variables on the total energy required for the process. These variables are molar fraction of CO_2 in the input gas, carbonation temperature, calcination temperature, gas

heat recovery effectiveness, and solid heat recovery effectiveness. The overall energy balance for the cycle per mole of CO_2 captured is given by

$$\bar{Q}_{\text{cycle}} = \frac{\Delta h^0_{\text{calc}} + \Delta h_{\text{ig}} + \Delta h_{\text{CaCO}_3} - \gamma_{\text{g}}\varepsilon_{\text{g}}(\Delta h_{\text{dg}} + \Delta h_{\text{CO}_2,T_0\to T_7} - \Delta h^0_{\text{carb}}) - \varepsilon_{\text{s}}\Delta h_{\text{CaO}} - \varepsilon_{\text{gs}}\Delta h_{\text{CO}_2,T_{\text{carb}}\to T_{\text{calc}}}}{n_{\text{CO}_2,\text{captured}}} \tag{2.2a}$$

$$\Delta h^0_{\text{calc}} = \sum n_{\text{p}}\bar{h}_{\text{p},T_{\text{calc}}} - \sum n_{\text{r}}\bar{h}_{\text{r},T_{\text{calc}}}, \quad \Delta h_{\text{CaCO}_3} = n_{\text{CaCO}_3}(\bar{h}_{\text{CaCO}_3,T_{\text{calc}}} - \bar{h}_{\text{CaCO}_3,T_{\text{carb}}}), \quad \Delta h_{\text{ig}} = \sum n_i(\bar{h}_{i,T_{\text{carb}}} - \bar{h}_{i,T_0}) \tag{2.2b}$$

$$\Delta h_{\text{dg}} = \sum n_j(\bar{h}_{j,T_{\text{carb}}} - \bar{h}_{j,T_0}), \quad \Delta h_{\text{CO}_2,T_0\to T_7} = n_{\text{CO}_2}(\bar{h}_{\text{CO}_2,T_7} - \bar{h}_{\text{CO}_2,T_0}), \quad \Delta h^0_{\text{carb}} = \sum n_{\text{p}}\bar{h}_{\text{p},T_{\text{carb}}} - \sum n_{\text{r}}\bar{h}_{\text{r},T_{\text{carb}}} \tag{2.2c}$$

$$\Delta h_{\text{CaO}} = n_{\text{CaO}}(\bar{h}_{\text{CaO},T_{\text{calc}}} - \bar{h}_{\text{CaO},T_{\text{carb}}}), \quad \Delta h_{\text{CO}_2,T_{\text{carb}}\to T_{\text{calc}}} = n_{\text{CO}_2}(\bar{h}_{\text{CO}_2,T_{\text{calc}}} - \bar{h}_{\text{CO}_2,T_{\text{carb}}}) \tag{2.2d}$$

where Δh^0_{calc}, Δh_{ig}, and Δh_{CaCO_3} are the total energy required for the calcination reaction, the total energy required to heat the input gas, and the total energy required to heat the $CaCO_3$ from the carbonation temperature to the calcination temperature. The terms containing Δh_{dg}, Δh_{CO_2}, Δh^0_{carb}, and Δh_{CaO} quantify energy that can be regained using gas and solid phase heat recovery. ε_{g}, ε_{s}, and ε_{gs} are the gas, solid, and gas–solid heat recovery effectiveness, respectively. For simplicity, ε_{gs} is assumed to be equal to ε_{s} in the following results. The coefficient γ_{g} is introduced to ensure the recovered heat does not exceed the maximum enthalpy change of the input gas [40], and is defined as

$$\gamma_{\text{g}} = \begin{cases} \xi_{\text{g}} \text{ for } \xi_{\text{g}} < 1 \\ 1 \text{ for } \xi_{\text{g}} \geq 1 \end{cases}, \tag{2.3a}$$

$$\xi_g = \frac{\Delta h_{\text{ig}}}{\varepsilon_{\text{g}}(\Delta h_{\text{dg}} + \Delta h_{\text{CO}_2,T_0\to T_7} - \Delta h^0_{\text{carb}})} \tag{2.3b}$$

The denominator of Eq. (2.3b) represents the available enthalpy that can be recovered from the CO_2-depleted gas, CO_2, and exothermic carbonation reaction. The numerator of Eq. 2.3b represents the total enthalpy change of the input gas from T_0 to T_{carb}. If $\xi_g < 1$, more heat is available in the gases undergoing cooling than is necessary to fully preheat the input gas. Thus, the gas heat recovery term in Eq. (2.2a), which is the same as the denominator of Eq. (2.3b), must be truncated by multiplying by γ_{g}. An alternative way of saying this is that when $\xi_g < 1$ the gas heat recovery term in Eq. (2.2a) becomes Δh_{ig}. A similar γ term is not needed for the solid and gas–solid heat recovery because the enthalpy change of $CaCO_3$ is always larger than the enthalpy change of CaO and CO_2 and thus no truncation is needed. For this reason, T_7, the temperature of the CO_2 after it is used to preheat the $CaCO_3$, is equal to T_{carb} unless $\varepsilon_{\text{gs}} = 0$, in which case T_7 is equal to T_{calc}.

The minimum solar input to the cycle per mole of CO_2 captured, $\overline{Q}_{\text{solar}}$, is estimated by considering the absorption efficiency of the solar receiver, assumed to be a perfectly insulated isothermal blackbody. Thus, the only heat losses are those associated with reradiation through the receiver aperture. With these assumptions, the absorption efficiency is

$$\eta_{\text{abs}} = \frac{\overline{Q}_{\text{cycle}}}{\overline{Q}_{\text{solar}}} = \frac{\overline{Q}_{\text{solar}} - \overline{Q}_{\text{rerad}}}{\overline{Q}_{\text{solar}}} = 1 - \frac{\sigma T_{\text{calc}}^4}{G_0 C} \tag{2.4}$$

where σ is the Stefan–Boltzmann constant, G_0 is the direct solar irradiation, and C is the solar concentration ratio [10].

For comparison purposes, the thermodynamic minimum separation work for a binary gas mixture of CO_2 and N_2, the maximum work that can be obtained by combustion of fossil fuels, and the maximum work that can be obtained using fossil fuels in an ideal fuel cell are determined (per mole of CO_2 in the input gas/produced in combustion/fuel cell) as

$$\overline{W}_{\min} = -\frac{\overline{R}T_0}{1000}\frac{\bar{x}_{CO_2}\ln\left(\bar{x}_{CO_2}\right)+\left(1-\bar{x}_{CO_2}\right)\ln\left(1-\bar{x}_{CO_2}\right)}{\bar{x}_{CO_2}} \tag{2.5}$$

$$\overline{W}_{c} = \left(1-\frac{T_0}{T_H}\right)\times\overline{\mathrm{HHV}}\,\frac{n_{fuel}}{n_{CO_2}} \tag{2.6}$$

$$\overline{W}_{fc} = -\Delta\bar{g}^{0}_{298K} = -\frac{\sum_i n_{i,p}\bar{g}_{i,p}-\sum_i n_{i,r}\bar{g}_{i,r}}{n_{CO_2}} \tag{2.7}$$

where $\bar{R}$ is the universal gas constant, T_0 is the ambient temperature, $\bar{x}_{CO_2}$ is the molar fraction of CO_2 being separated from the mixture, $\overline{\mathrm{HHV}}$ is the higher heating value of the fuel, T_H is the adiabatic flame temperature, and $\bar{g}$ is the Gibbs function [41,42]. Mixing is assumed to take place isothermally and isobarically.

2.4 Results

The following results are evaluated using the baseline parameters listed in Table 2.2 unless otherwise indicated. Figure 2.2 shows the minimum work per mole of CO_2 captured required to separate CO_2 from an ideal binary gas mixture as a function of the CO_2 molar fraction in the input gas as calculated with Eq. (2.5). At CO_2 molar fractions

below 0.0008, the work required exceeds $20\ \text{kJ mol}^{-1}_{\text{CO}_2\ \text{captured}}$ and decreases quickly with increasing $\bar{x}_{0,\text{CO}_2}$, reaching $7\ \text{kJ mol}^{-1}_{\text{CO}_2\ \text{captured}}$ at $\bar{x}_{0,\text{CO}_2} = 0.15$.

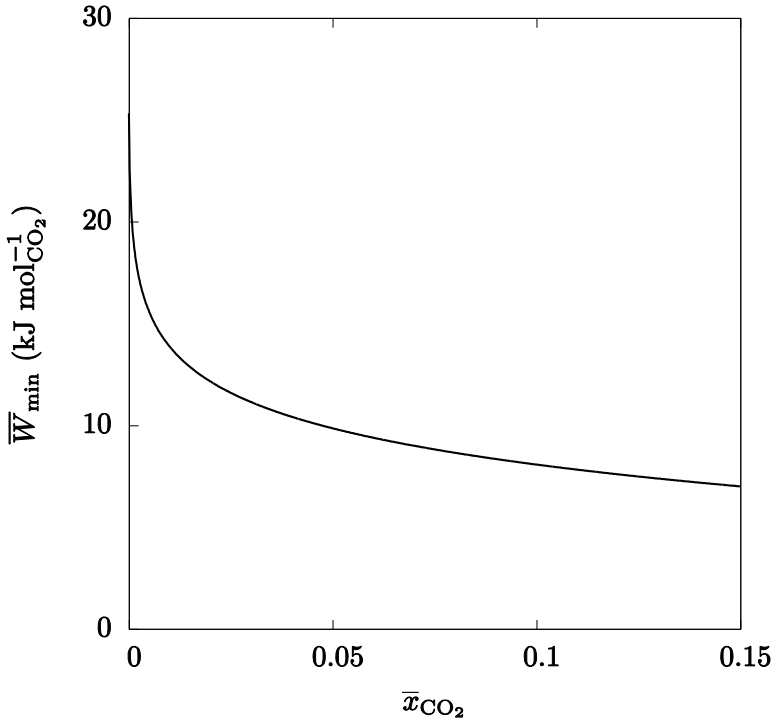

Figure 2.2: Thermodynamic minimum work of CO_2 separation per mole of CO_2 captured from a binary ideal gas mixture as a function of the input CO_2 molar fraction, $\bar{x}_{0,\text{CO}_2}$

The solar energy input per mole of CO_2 captured, $\bar{Q}_{\text{solar}}$, required to drive the cycle as a function of CO_2 molar fraction in the input gas is shown in Fig. 2.3 and follows the trend anticipated based on the results of Fig. 2.2. Figure 2.3a shows $\bar{Q}_{\text{solar}}$ for 0% solid heat recovery and varying gas heat recovery, but the shape of the curve is the same for all values of solid heat recovery. The required solar input is greater than $45\ \text{MJ mol}^{-1}_{\text{CO}_2\ \text{captured}}$ for low CO_2 molar fractions and drops off quickly, reaching a minimum value of

$283\ \text{kJ mol}^{-1}_{\text{CO}_2\ \text{captured}}$ for 100% gas heat recovery and 0% solid heat recovery, $303\ \text{kJ mol}^{-1}_{\text{CO}_2\ \text{captured}}$ for 100% solid heat recovery and 0% gas heat recovery, and $207\ \text{kJ mol}^{-1}_{\text{CO}_2\ \text{captured}}$ for both gas and solid heat recovery of 100%. The required solar input is high at low CO_2 molar fractions mainly due to the large amount of inert gas that is heated to T_{carb}. For 100% gas heat recovery, $\bar{Q}_{\text{solar}}$ is constant for all CO_2 molar fractions because the exit streams can fully preheat the input gas to T_{carb}. The other two contributions to $\bar{Q}_{\text{solar}}$ are heating $CaCO_3$ from T_{carb} to T_{calc} and the calcination reaction enthalpy, neither of which are functions of CO_2 concentration, so $\bar{Q}_{\text{solar}}$ is constant. Gas heat recovery can reduce $\bar{Q}_{\text{solar}}$ by 22–99% depending on the CO_2 molar fraction, with the largest benefit gained at low CO_2 molar fractions. Figure 2.3b shows $\bar{Q}_{\text{solar}}$ for 0% gas heat recovery and varying solid heat recovery. The shape of the curve is the same for all values of gas heat recovery except $\varepsilon_{\text{g}} = 1$, and the heat requirements decrease with increasing CO_2 molar fraction. As mentioned previously, at 100% gas heat recovery $\bar{Q}_{\text{solar}}$ is constant and independent of CO_2 molar fraction; increasing the solid heat recovery simply reduces the constant value from $283\ \text{kJ mol}^{-1}_{\text{CO}_2\ \text{captured}}$ to $207\ \text{kJ mol}^{-1}_{\text{CO}_2\ \text{captured}}$. Solid heat recovery can lower $\bar{Q}_{\text{solar}}$ by 0.1–26%, with the largest benefit gained at high CO_2 molar fractions.

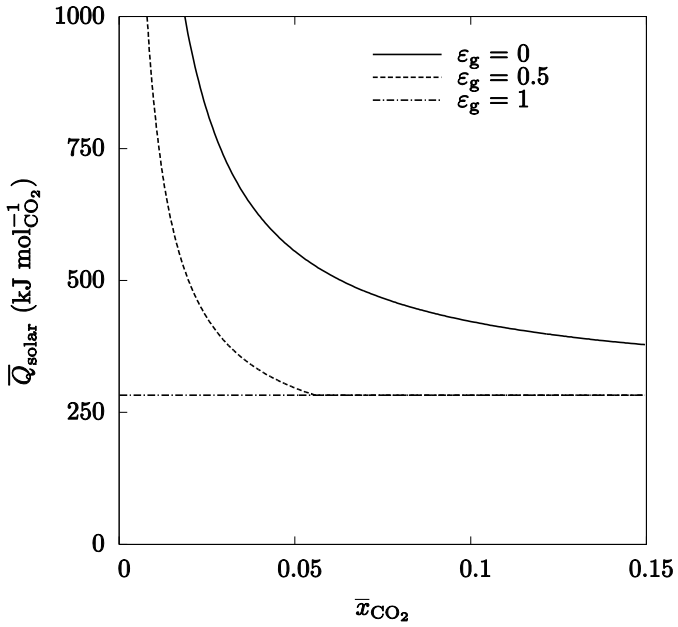

(a)

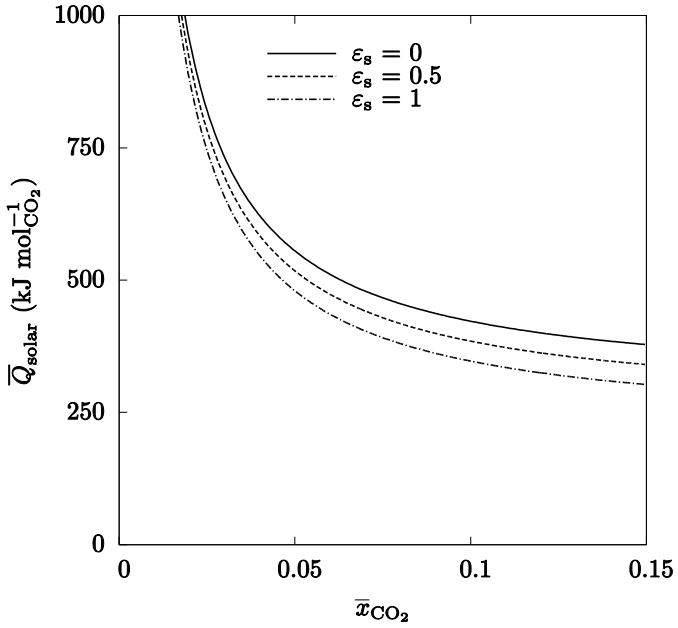

(b)

Figure 2.3: Effect of the molar fraction of CO_2 in the input gas, $\overline{x}_{0,CO_2}$, on the amount of heat required to separate 1 mole of CO_2 for (a) $\varepsilon_s = 0$ and selected values of gas heat recovery, and (b) for $\varepsilon_g = 0$ and selected values of solid heat recovery.

The effect of CO_2 molar fraction in the input gas on the solar energy input per mole of CO_2 captured at the various levels of gas and solid heat recovery outlined in Fig. 2.3 can be explained by the relative contributions of heating the input gas, heating the $CaCO_3$, and the calcination reaction enthalpy on the total cycle heat requirement, shown in Fig. 2.4. At very low CO_2 molar fractions, the energy required to heat the input gas makes up nearly all of the heat required for the cycle, and gas heat recovery is more effective. In contrast, as the CO_2 molar fraction increases, the fraction of heat required to heat the solid $CaCO_3$ also increases, and solid heat recovery becomes equally important.

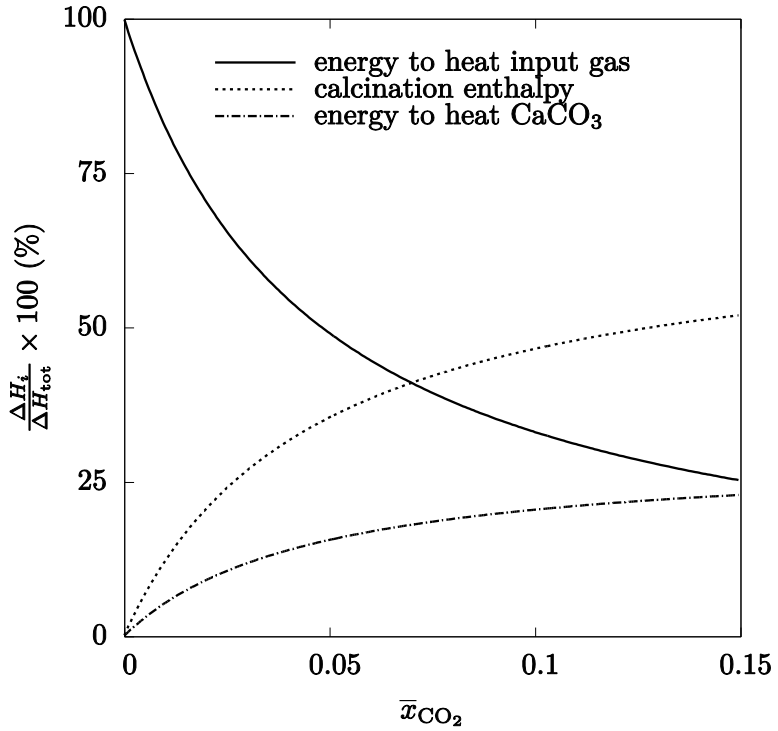

Figure 2.4: Relative contributions of heating input gas, heating $CaCO_3$, and calcination enthalpy to the cycle heat requirements per mole of CO_2 captured.

The effect of varying the carbonation temperature and gas heat recovery for a CO_2 molar fraction of 0.1—a midrange value for the different power plant types in Table

2.1—on $\bar{Q}_{solar}$ and the equilibrium partial pressure of CO_2 is shown in Fig. 2.5a. The results show a gradual increase of $\bar{Q}_{solar}$ with increasing carbonation temperature for 0% gas heat recovery until about 900 K, at which point $\bar{Q}_{solar}$ increases sharply. This is due to the increasing equilibrium molar fraction of CO_2 as the temperature increases. Because the input molar fraction of CO_2 is constant, as the equilibrium molar fraction approaches the input molar fraction very little CaO is carbonated, resulting in very little CO_2 captured during the cycle. At 100% gas heat recovery, $\bar{Q}_{solar}$ decreases with increasing T_{carb}. The input gas has been fully preheated by the exiting gases, so increasing T_{carb} decreases the energy required to heat $CaCO_3$ from T_{carb} to T_{calc}, relaxing the requirements for the heat recovery between CaO and $CaCO_3$, and consequently decreasing the overall hat requirements for a given ε_s. The same trend was observed for all values of CO_2 molar fraction studied. Figure 2.5b and c show the effect of varying the carbonation temperature and solid heat recovery on $\bar{Q}_{solar}$ for a CO_2 molar fraction of 0.1. Figure 2.5b shows $\bar{Q}_{solar}$ for 0% gas heat recovery and Fig. 2.5c shows 100% gas heat recovery. The trends shown in Fig. 2.5b are similar to those of Fig. 2.5a, a gradual increase in $\bar{Q}_{solar}$ with increasing carbonation temperature and a sharp increase around 900 K. Figure 2.5c shows a decrease in $\bar{Q}_{solar}$ with increasing carbonation temperature for all values of solid heat recovery, similar to the curve for $\varepsilon_s = 1$ in Fig. 2.5a.

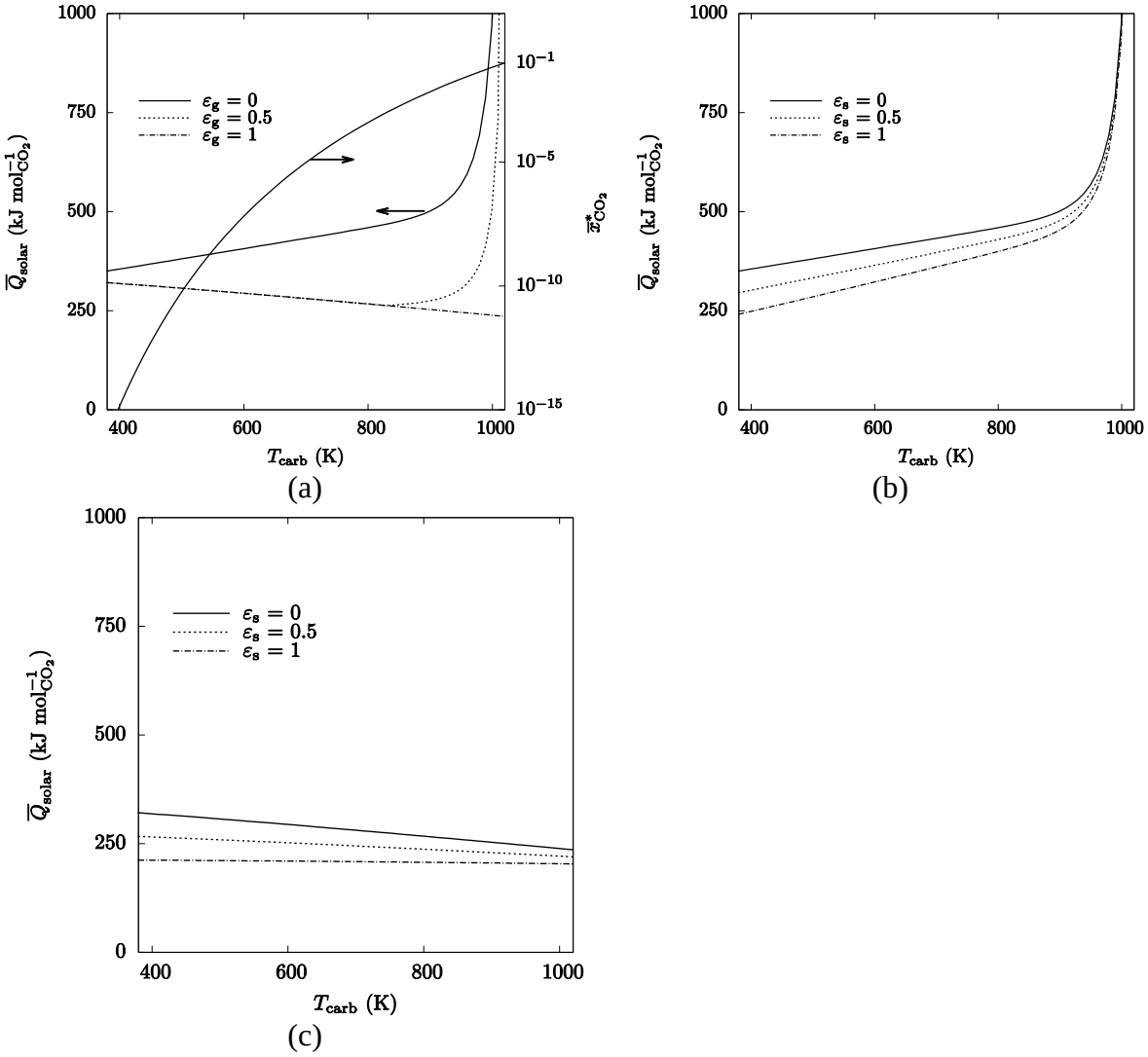

Figure 2.5: Effect of carbonation temperature on (a) heat requirements per mole of CO_2 captured and equilibrium CO_2 molar fraction for $\varepsilon_s = 0$ and selected values of gas heat recovery, (b) heat requirements per mole of CO_2 captured for $\varepsilon_g = 0$ and selected values of solid heat recovery, and (c) heat requirements per mole of CO_2 captured for $\varepsilon_g = 1$ and selected values of solid heat recovery.

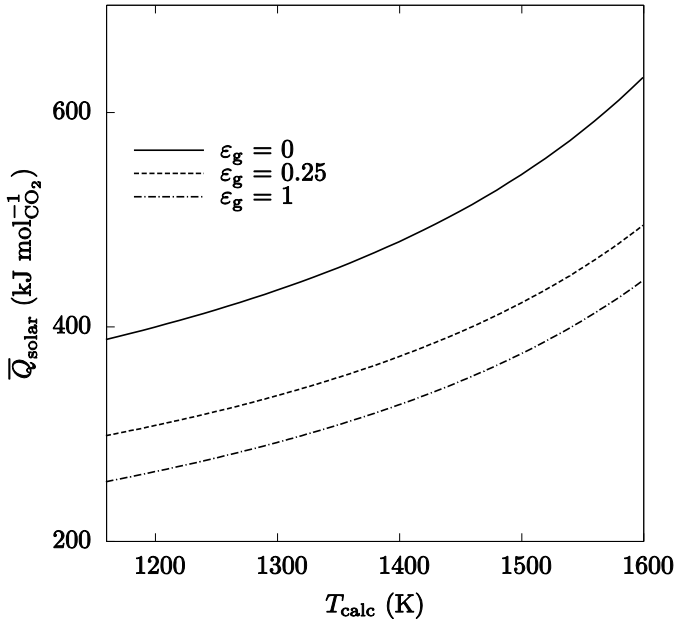

(a)

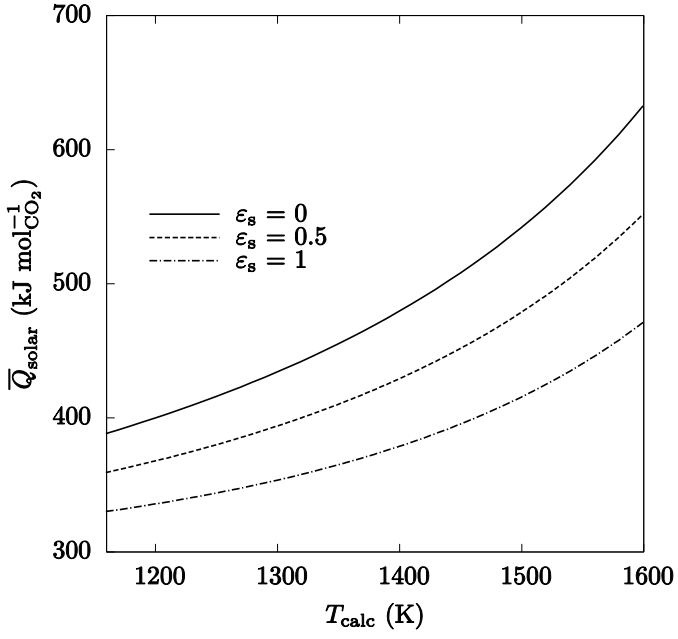

(b)

Figure 2.6: Effect of calcination temperature on heat requirements per mole of CO_2 captured for (a) $\varepsilon_s = 0$ and selected values of gas heat recovery and (b) $\varepsilon_g = 0$ and selected values of solid heat recovery.

Next, the effect of varying the calcination temperature is studied. Cycle heat requirements for a CO_2 molar fraction of 0.1 are shown in Fig. 2.6a for $\varepsilon_s = 0$ and selected values of ε_g. The required solar input increases monotonically with calcination temperature. Unlike the carbonation reaction, the calcination reaction is unaffected by the equilibrium partial pressure of CO_2 at the temperatures and pressures studied. The shape of the curve is the same for all values of CO_2 molar fraction and solid heat recovery. Figure 2.6b shows the effect of varying calcination temperature and solid heat recovery for $\varepsilon_g = 0$ and selected values of ε_s on $\bar{Q}_{solar}$. The behavior is similar to Fig. 2.6a, although the values are slightly higher due to the greater importance of gas heat recovery as shown in Fig. 2.4. The shape of the curves in both Fig. 2.6a and b is influenced by the decreasing absorption efficiency due to increasing T_{calc}, whereas in previous figures the absorption efficiency was constant.

Finally, Table 2.3 shows the higher heating values and maximum work per mole of CO_2 produced that can be achieved from various hydrocarbon fuels [43]. It is clear when comparing the values in Table 2.3 to Fig. 2.3 that the heat requirements for the $CaCO_3$ cycle at atmospheric molar fractions of CO_2 and low values of gas heat recovery far exceed the total available heat from burning hydrocarbon fuels. If these fuels were used to supply heat for the cycle, burning them would produce more CO_2 than the amount captured. While using concentrated solar to supply heat to the cycle would eliminate this problem, it gives a sense of scale for how much heat is needed to separate CO_2 at very low molar fractions with low or no heat recovery. The high heat required would also

require a very large heliostat field, greatly increasing the cost of any real installation operating the cycle and thus increasing the price of electricity. However, for 100% gas heat recovery the cycle requires 20-70% of the total available heat from the fuels.

Table 2.3: Maximum work available per mole of CO_2 produced from selected hydrocarbon fuels [43].

Fuel	$\overline{HHV}$ ($kJ\ mol_{fuel}^{-1}$)	Adiabatic flame temperature (K)	Carnot work ($kJ\ mol_{CO_2}^{-1}$)	Maximum fuel cell work ($kJ\ mol_{CO_2}^{-1}$)
carbon	394	2473	346	395
methane	888	2223	770	818
octane	5392	2395	590	663

2.5 Summary

A thermodynamic analysis of the CaO–based carbonation–calcination process was conducted to determine the effect of reaction temperature, gas and solid heat recovery, and inlet gas CO_2 concentration on the total solar heat required for the process. The heat requirements to capture atmospheric levels of CO_2 with this process are prohibitively high, over 45 MJ per mole of CO_2 captured with no heat recovery. However, it is well matched to higher CO_2 concentrations such as those found in power plant flue gas, with heat requirements as low as 207 kJ per mole of CO_2 captured with perfect gas and solid heat recovery. Gas phase heat recovery can reduce $\overline{Q}_{solar}$ by 22 to 99%, with the largest gains occurring at lower CO_2 molar fractions. Solid phase heat recovery can reduce $\overline{Q}_{solar}$ by 0.1 to 26%, with the largest gains occurring at higher CO_2 molar fractions. In most cases, lower reaction temperatures result in reduced heat requirements.

Although gas phase heat recovery is important in the overall energy balance, it can be implemented externally to the reactor vessel using commercially available heat exchangers. Solid phase heat recovery is of smaller importance, and its implementation would add considerable complexity to the reactor design. For these reasons, the reactor concepts shown in subsequent chapters do not consider either form of heat recovery. The reactor is designed to study the CO_2 concentration range of 5–15%, as this analysis has shown that the selected process is not suitable to atmospheric CO_2 concentrations.

CHAPTER 3: REACTOR CONCEPT DEVELOPMENT

The basic design requirements of the reactor include the ability to withstand temperature cycling between 25°C and 1100°C in gas atmospheres that contain CO_2 (10-100%), N_2 (0-90%), and steam (0-20%). The parts of the reactor in contact with the reacting particles should not react with CaO, $CaCO_3$, or $Ca(OH)_2$. The gas flow paths should be sealed from the rest of the reactor in order to obtain accurate measurements of gas flow rates. In addition, thermocouples should be located throughout the reactor in order to monitor experimental conditions and validate the numerical model. Guided by the results of the thermodynamic analysis, three different reactor concepts are examined for their heat and mass transfer characteristics. These reactor concepts are shown in Fig. 3.1. Concept 1 has a horizontally oriented axis with the aperture on the side, concept 2 has a vertically oriented axis with the aperture on the side, and concept 3 has a vertically oriented axis with the aperture on the bottom. The three concepts share some common features. All are indirectly irradiated and windowless. Radiation absorbed at the cavity wall is transferred by conduction to the annular space formed by the two cylindrical walls. The annular space is filled with a reacting packed bed of $CaCO_3$ particles. It is a batch process in which each consecutive reaction is performed. The particles remain inside the reactor throughout the process as the gas species are changed and solar input is switched on and off to drive each reaction. In an industrial scale version of this reactor, the calcination step could be performed during the day and the carbonation reaction at night. Alternatively, the carbonation step could be performed off-sun in a separate

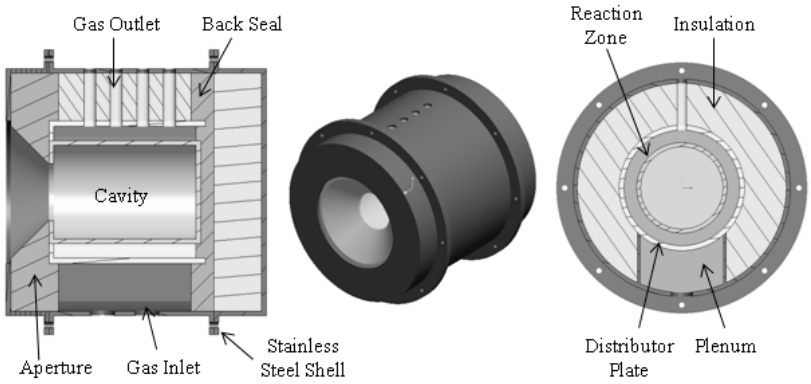

Figure 3.1a: Reactor concept #1 (left: side cross section, middle: trimetric view, right: front cross section) [44]

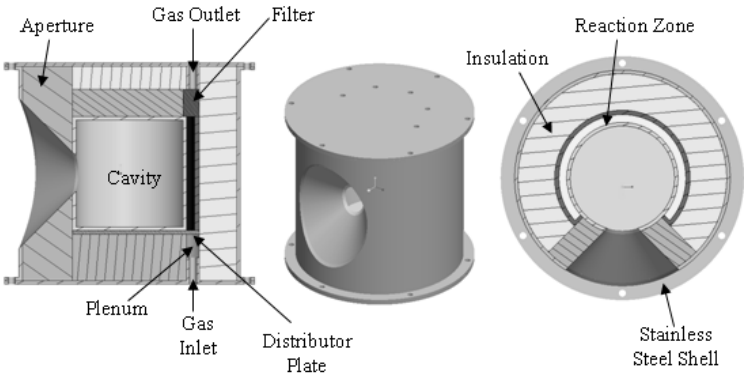

Figure 3.1b: Reactor concept #2 (left: side cross section, middle: trimetric view, right: top cross section) [44]

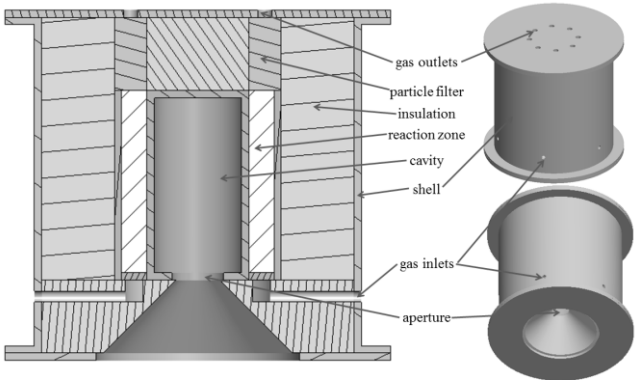

Figure 3.1c: Reactor concept #3 (left: side cross section, top right: top trimetric view, bottom right: bottom trimetric view) [45]

reactor. Gas enters the reactor via inlets into a plenum then passes through a distributor plate and into the reaction zone. The distributor plate is designed to achieve a uniform velocity distribution across the bottom of the annulus. The plate is also removable, allowing plates with different hole layouts and sizes to be used depending on the conditions of the experiment. The gas flows through the annular reaction zone and exits the reactor through outlets at the top.

The three concepts have advantages and disadvantages when compared to one another. Concepts 1 and 3 are likely easier to manufacture than concept 2, particularly the aperture and cavity pieces. Securing the cavity and annular walls in place is a challenge in concept 1, while the cavity and annular walls in concepts 2 and 3 can be simply supported by ceramic insulation. Fluidized and packed beds of particles with a vertical annular reaction zone like in concepts 2 and 3 have been operated successfully and correlations exist for the design of the plenum and distributor plate of such beds [46]. The cavity of concept 2 has a large amount of surface area not in direct contact with the reaction zone, which could result in high temperature gradients and thermal stresses. The cavity design of concepts 1 and 3 is common to solar-driven reactors, and the expected reradiation and convection losses from such a cavity are easily quantified [47,48]. The beam up configuration of concept 3 reduces convective losses through the open aperture when compared to the horizontal cavity of concept 1 [49,50]. When a reactor is inclined to the horizontal, a larger recirculation zone forms in the cavity and reduces inflow of cooler air from the environment, reducing convective losses [47]. For these reasons,

concept 3 was chosen for further refinement. It has the most advantages and the lowest number of anticipated design challenges when compared to the other two concepts. Subsequent chapters describe the thermal and mechanical analyses used to transform the concept into a complete engineering design ready to manufacture.

CHAPTER 4: STEADY STATE HEAT AND MASS TRANSFER MODEL[2]

4.1 Introduction

After the initial concept selection, the next important step in the design process is to establish the overall dimensions of the reactor. The cavity dimensions are particularly important, as their selection affects both the radiative and convective heat losses through the open aperture of the reactor. This chapter describes a numerical model of heat and mass transfer in the cavity and reaction zone of the chosen reactor concept. The cavity geometry is varied to determine its effects on the temperature and velocity profiles in the reactor and on the work required to pump gases through the reaction zone. Two different methods are used to determine the net radiative flux at the cavity walls, and the computation time and accuracy are compared.

4.2 Problem Statement

A cross section of the three dimensional computational domain used for the calculations is shown in Fig. 4.1. For simplicity, only the reaction zone and reactor cavity are modeled. The cavity height is H, r_{cav} is the inner radius of the cavity, r_1 is the outer radius of the cavity and the inner radius of the reaction zone, and r_2 is the outer radius of

[2] Material in this chapter has been published in L. Reich, R. Bader, T. Simon, and W. Lipiński. Thermal Transport Model of a Packed-Bed Reactor for Solar Thermochemical CO_2 Capture. *Special Topics and Reviews in Porous Media* (in press), 2015 [45].

the reaction zone. The reaction zone is modeled as a homogeneous, radiatively-participating porous medium with local thermal equilibrium between the gas (CO_2) and solid ($CaCO_3$) phases. The cavity wall is modeled as an opaque, isotropic solid. The steady-state conservation equations are iteratively solved until conversion is reached. External body forces, including gravity, are neglected.

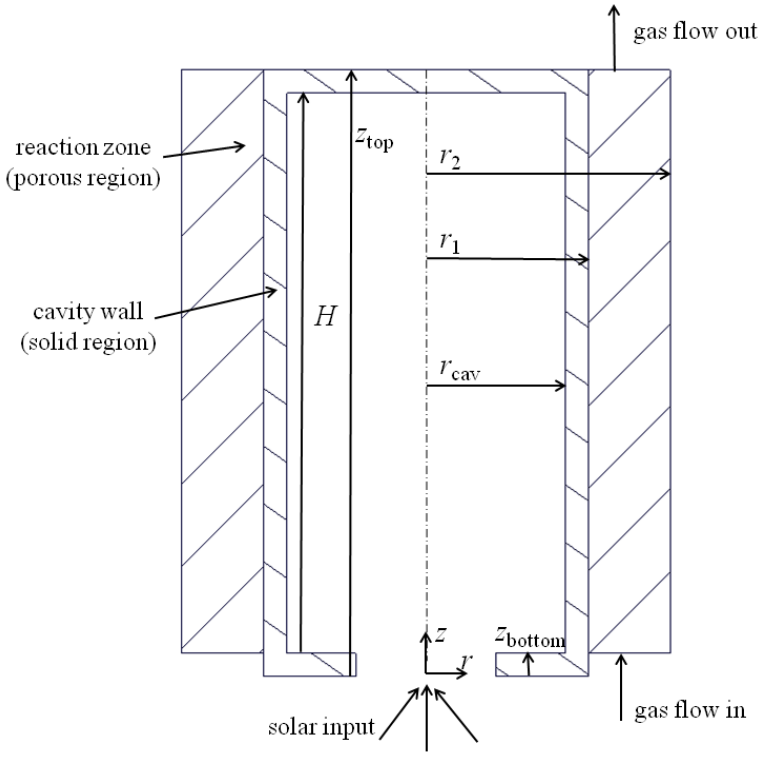

Figure 4.1: Schematic of the computational domain used in the steady state analysis

The reaction zone is a packed bed with a particle volume fraction, $f_{v,s}$, of 0.7. The dimensions of the reactor are varied to study their effects on the temperature and velocity distributions in the reaction zone. In these calculations, the reaction zone volume is held constant as the cavity height and diameter are varied. The maximum volume of the reaction zone is calculated by assuming a particle volume fraction of $f_{v,s} = 0.1$ to allow

for optional reactor operation as a fluidized bed, a solar input power $q_{\text{solar}} = 1\ \text{kW}$, a solar-to-chemical conversion efficiency $\eta = \dfrac{M_{\text{CaO}} \Delta \bar{h}^{0}_{\text{calc}}}{\bar{M}_{\text{CaO}} q_{\text{solar}} t} = 0.35$, and a calcination time of 30 minutes. The particle size and the volume fraction of particles in the reaction zone are assumed to be unchanged during the carbonation–calcination process. Using these assumptions, the mass of CaO produced by calcination is 196.5 g. The reaction zone volume is then given by $V_{\text{r}} = \dfrac{V_{\text{CaO}}}{f_{\text{v,s}}} = \dfrac{M_{\text{CaO}}}{\rho_{\text{CaO}} f_{\text{v,s}}} = 586.5\ \text{cm}^3$. This is the anticipated maximum reaction zone volume. For fixed nominal reactor thermal power and decreasing reacting efficiency, the reaction zone volume decreases for a given reaction time. The base case values and the ranges of parameters investigated in this study are shown in Table 4.1. The range of cavity dimensions was established by calculating the absorption efficiency for a wide variety of cavity dimensions and eliminating those with an efficiency of less than 90% as well as those with a cavity too large to accommodate the selected reaction zone volume.

Table 4.1: Base case and ranges of parameters investigated in the steady state analysis

Parameter	Symbol	Unit	Baseline value	Value range
Cavity radius	r_{cav}	cm	3	2–6
Length-to-radius ratio	H/r_{cav}	–	4	4–6
Heat loss	q''_{wall}	–	0	$0 - 0.2\dfrac{q_{\text{solar}}}{2\pi r_2 H}$

The solar radiative flux entering the cavity is assumed to be uniformly distributed within a cone angle of 45° with a total power of 1 kW and a concentration ratio of 1000. The cone angle matches that typical of solar concentrators and of the solar simulator where the reactor will be tested [51]. Only the solar step of the process is considered in this chapter, and chemical reaction effects are neglected.

4.3 Governing Equations

The heat and mass transfer model is based on the mass, momentum and energy conservation equations [52]. Using the above assumptions and applying them to the packed bed region, these equations reduce to:

Continuity: $$\nabla \cdot \left(\rho \vec{\mathbf{v}} \right) = 0 \tag{4.2}$$

Momentum: $$\nabla \cdot \left(\rho \vec{\mathbf{v}} \vec{\mathbf{v}} \right) = -\nabla p + \nabla \cdot \left(\bar{\bar{\boldsymbol{\tau}}} \right) + \vec{\mathbf{S}} \tag{4.3}$$

Energy: $$\nabla \cdot \left[\vec{\mathbf{v}} \left(\rho_{\mathrm{f}} E_{\mathrm{f}} + p \right) \right] = -\nabla \cdot \vec{\mathbf{q}}''_{\mathrm{rad}} + \nabla \cdot \left[k_{\mathrm{eff}} \vec{\nabla} T + \left(\bar{\bar{\boldsymbol{\tau}}} \cdot \vec{\mathbf{v}} \right) \right] \tag{4.4}$$

where ρ is density, $\vec{\mathbf{v}}$ is the superficial fluid velocity vector, $\vec{\mathbf{S}}$ is a momentum source term, $\bar{\bar{\boldsymbol{\tau}}}$ is the shear stress tensor, p is the static pressure, and E is the internal plus kinetic energy term, $E = h - \frac{p}{\rho} + \frac{v^2}{2}$; v is the fluid speed, $\vec{\mathbf{q}}''_{\mathbf{rad}}$ is the internal radiative heat flux, k_{eff} is the effective thermal conductivity determined using the homogenous model, $k_{\mathrm{eff}} = (1 - f_{\mathrm{v,s}}) k_{\mathrm{f}} + f_{\mathrm{v,s}} k_{\mathrm{s}}$, T is temperature, h is enthalpy, and the subscripts f and s indicate fluid and solid, respectively.

For a homogeneous porous medium, the source term in Eq. (4.3) accounts for viscous and inertial losses and is calculated using

$$\vec{\mathbf{S}} = -\left(\frac{\mu}{K}\vec{\mathbf{v}} + \frac{1}{2}C_{\mathrm{f}}\rho\left|\vec{\mathbf{v}}\right|\vec{\mathbf{v}} \right) \tag{4.5}$$

where K is the permeability and C_{f} is the Forchheimer coefficient of the porous zone. The Ergun equation is used to derive K and C_{f} for the packed bed, resulting in $\frac{1}{K} = \frac{150\, f_{\mathrm{v,s}}^2}{D_{\mathrm{p}}^2(1-f_{\mathrm{v,s}})^3}$ and $C_{\mathrm{f}} = \frac{3.5\, f_{\mathrm{v,s}}}{D_{\mathrm{p}}(1-f_{\mathrm{v,s}})^3}$ [53]. In these calculations, $f_{\mathrm{v,s}}$ is 0.7 and D_{p} is 100 μm. The particle volume is assumed to be unchanged. During the calcination reaction, a particle becomes more porous, and the particle radius shrinks by only 3-5% [22]. As the particles are calcined and carbonated over many cycles, they sinter and shrink. The particle shrinking is expected to increase the pressure drop, but without considerable effects on temperature and heat transfer rates. The typical range of solid volume fraction values for monodisperse, randomly-packed spheres is 0.56–0.64 with a maximum of 0.74 for cubic or hexagonal close-packed spheres [54]. A higher value was chosen as, in reality, the particles will not be completely spherical or monodisperse, resulting in increased solid volume fraction. In the silicon carbide cavity wall region, the energy equation reduces to:

$$-k_{\mathrm{SiC}}\nabla^2 T = 0 \tag{4.6}$$

where k_{SiC} is the thermal conductivity of the cavity wall.

The divergence of the radiative heat flux in the packed bed is found by solving the radiative transfer equation, which, for a gray medium, reduces to [48]:

$$\nabla\cdot\vec{\mathbf{q}}''_{\mathrm{rad}} = \kappa\left(4\sigma T^4 - \int_{\lambda=0}^{\infty}\int_{\Omega=0}^{4\pi} I_\lambda(\hat{\mathbf{s}})\mathrm{d}\Omega \right) \tag{4.7}$$

For the range of dimensions and radiative properties of the reactive medium considered in this study (see Table 4.2 and section 4.4), the minimum optical thickness, τ, is over 20,000 and the packed bed medium is optically thick. Consequently, the Rosseland diffusion approximation is employed to model the internal radiative heat transfer in the packed bed, although the approximation is known to fail at boundaries [48,55,56]. It approximates the radiative transfer in an optically thick, isotropically scattering medium as a conduction problem with highly temperature dependent thermal conductivity. Particles of $CaCO_3$ are assumed to absorb and independently scatter radiation. The CO_2 is assumed to be radiatively nonparticipating, as the maximum optical thickness of 0.6 is negligible compared to the optical thickness of the particles. Thus, in Eq. (4.4) the radiative heat flux can be approximated by $\vec{\mathbf{q}}''_{\text{rad}} = -k_{\text{rad}} \nabla T$, where $k_{\text{rad}} = \frac{16 n^2 \sigma T^3}{3(\kappa + \sigma_s)}$, n is the real part of the refractive index of the host medium, κ is the absorption coefficient, and σ_s is the scattering coefficient. The scattering and absorption coefficients are calculated assuming independent scattering using Mie theory with a characteristic particle diameter of 100 μm [57]. The spectral values of the complex refractive index, m, of $CaCO_3$ are used to obtain κ_λ and $\sigma_{s,\lambda}$; then, since the values are nearly constant across the spectrum, κ_λ and $\sigma_{s,\lambda}$ are algebraically averaged over the spectrum to obtain κ and σ_s.

4.4 Boundary Conditions

The boundary conditions are

- For the continuity equation:

$$\rho_{\mathrm{f}}\left(\vec{\mathbf{v}}\cdot\hat{\mathbf{k}}\right)\Big|_{r_1<r<r_2,\,z=z_{\mathrm{bottom}}} = \rho_{\mathrm{f}} u_{z,\mathrm{in}} \tag{4.8}$$

- For the momentum equation:

$$p\big|_{r_1<r<r_2,\,z=z_{\mathrm{top}}} = 0 \tag{4.9}$$

$$u_r\big|_{r=r_1,\,z_{\mathrm{bottom}}<z<z_{\mathrm{top}}} = u_r\big|_{r=r_2,\,z_{\mathrm{bottom}}<z<z_{\mathrm{top}}} = u_z\big|_{r=r_1,\,z_{\mathrm{bottom}}<z<z_{\mathrm{top}}} = u_z\big|_{r=r_2,\,z_{\mathrm{bottom}}<z<z_{\mathrm{top}}} = 0 \tag{4.10}$$

- For the energy equation:

$$T\big|_{r_1<r<r_2,\,z=z_{\mathrm{bottom}}} = T_{\mathrm{in}} \tag{4.11}$$

$$\left.\frac{\partial T}{\partial z}\right|_{0\le r\le r_1,\,z=0} = \left.\frac{\partial T}{\partial z}\right|_{0\le r\le r_1,\,z=z_{\mathrm{top}}} = 0 \tag{4.12}$$

$$-k_{\mathrm{SiC}}\left.\frac{\partial T}{\partial r}\right|_{r=r_{\mathrm{cav}},\,z_{\mathrm{bottom}}\le z\le H} = -k_{\mathrm{SiC}}\left.\frac{\partial T}{\partial z}\right|_{0\le r\le r_{\mathrm{cav}},\,z=H} = -k_{\mathrm{SiC}}\left.\frac{\partial T}{\partial z}\right|_{0\le r\le r_{\mathrm{cav}},\,z=z_{\mathrm{bottom}}} = q''_{\mathrm{rad}} \tag{4.13}$$

$$k_{\mathrm{SiC}}\left.\frac{\partial T}{\partial r}\right|_{r=r_1,\,z_{\mathrm{bottom}}\le z\le z_{\mathrm{top}}} = \left(k_{\mathrm{eff}} + k_{\mathrm{rad}}\right)\left.\frac{\partial T}{\partial r}\right|_{r=r_1,\,z_{\mathrm{bottom}}\le z\le z_{\mathrm{top}}} \tag{4.14}$$

$$-\left(k_{\mathrm{eff}} + k_{\mathrm{rad}}\right)\left.\frac{\partial T}{\partial r}\right|_{r=r_2,\,z_{\mathrm{bottom}}\le z\le z_{\mathrm{top}}} = q''_{\mathrm{wall}} \tag{4.15}$$

where u_z and u_r are the axial and radial components of velocity, T_{in} is the inlet temperature, q''_{rad} is the radiative flux profile on the cavity wall, and q''_{wall} is the heat flux at the outer wall of the reaction zone. The baseline values for each boundary condition

are listed in Table 4.3 at the beginning of section 4.7. The upper value of $q''_{\text{wall}} = 0.2\frac{q_{\text{solar}}}{2\pi r_2 H}$ was chosen to cover the full range of what might be expected for this reactor, based on previous studies reporting 9–13% conduction losses [36,37].

4.5 Thermophysical Properties

The physical properties of CO_2 and $CaCO_3$ are obtained from the ANSYS Fluent materials database [58]. The complex refractive index of $CaCO_3$ is obtained from the literature [59]. The physical properties of the SiC cavity walls are taken from CoorsTek data for reaction bonded silicon carbide and are assumed not to vary with temperature [60]. The emissivity, ε, of SiC comes from Toloukian [61]. Specific values of thermophysical properties are in Table 4.2.

4.6 Numerical Solution

The finite volume technique as implemented in the computational fluid dynamics (CFD) software ANSYS Fluent 15.0 is used to solve the conservation equations on a mesh with approximately 150,000 cells. The continuity equation is solved using the projection method and the SIMPLE segregated pressure–velocity coupling algorithm [62,63]. The momentum and energy equations are solved with a second-order upwind scheme. Gradients are evaluated using a least squares cell-based discretization scheme. Mesh independence is checked by increasing the number of CFD cells to about 300,000. This changes the solution by less than 5% for all parameters of interest.

Table 4.2: Thermophysical properties of materials in the steady state analysis

Property	Material		
	$CaCO_3$	CO_2	SiC
ρ (kg m^{-3})	2800	1.78	3100
k[3] (W m^{-1} K^{-1})	2.25	0.0145	125
c_p (J kg^{-1} K^{-1})	856	429.93 J kg^{-1} K^{-1}+1.87 J kg^{-1} K^{-2} T– 1.97x10^{-3} J kg^{-1} K^{-3} T^2 +1.297251x10^{-6} J kg^{-1} K^{-4} T^3 –4.00x10^{-10} J kg^{-1} K^{-5} T^4 (300–1000K) 841.38 J kg^{-1} K^{-1}+0.59 J kg^{-1} K^{-2} T –2.42x10^{-4} J kg^{-1} K^{-3} T^2 +4.52x10^{-8} J kg^{-1} K^{-4} T^3 –3.15x10^{-12} J kg^{-1} K^{-5} T^4 (1000-5000K)	800
ε	–	–	0.9
m	$1.55+\begin{cases}0.004\exp\left(-10\mu m^{-2}\lambda^2\right)\\ +0.1\exp\left[0.2\mu m^{-2}\left(\lambda^2-9\mu r\right.\right.\end{cases}$	–	–

The radiation in the reactor cavity is modeled using both the Monte Carlo (MC) ray-tracing method and the net radiation method (NRM) [48]. The computational times and accuracy of the two methods are compared.

The in-house developed Monte Carlo subroutine calculates the net heat flux at the inner cavity wall due to the solar source and reradiation inside the cavity [64]. The power of each ray and the number of rays launched at the aperture and the emitting cavity wall elements are calculated using:

[3] At 20°C.

$$q_{\text{ray}} = \frac{q_{\text{solar}} + \varepsilon\sigma\sum_i A_i T_i^4}{N_{\text{rays}}},\ N_{\text{solar}} = \frac{q_{\text{solar}}}{q_{\text{ray}}},\ N_i = \frac{\varepsilon\sigma A_i T_i^4}{q_{\text{ray}}} \tag{4.16}$$

where A_i is the emitting surface element area and N_{rays} is the total number of rays. The location and direction of a ray at the aperture assuming uniform emission are calculated as:

$$\vec{\mathbf{r}} = \left[r\cos\phi, r\sin\phi, z_{\text{bottom}}\right],\ r = r_{\text{ap}}\sqrt{\Re},\ \phi = 2\pi\Re \tag{4.17}$$

where $\Re$ is a randomly generated number between 0 and 1.

The direction of the ray launched at the aperture is obtained from:

$$\hat{\mathbf{u}} = \left[\sin\theta\cos\psi, \sin\theta\sin\psi, \cos\theta\right],\ \theta = \sin^{-1}\left(\sin\frac{\pi}{4}\sqrt{\Re}\right),\ \psi = 2\pi\Re \tag{4.18}$$

The location of ray emission by the cavity wall elements is obtained from

- for top and bottom surfaces

$$\vec{\mathbf{r}} = \left[r\cos\phi, r\sin\phi, \left\{H \text{ or } z_{\text{bottom}}\right\}\right],\ r = \sqrt{\Re\left(r_i^2 - r_{i-1}^2\right) + r_{i-1}^2},\ r_i = \frac{r_{\text{cav}} i}{n_r},\ \phi = 2\pi\Re \tag{4.19}$$

- for the cylindrical surface

$$\vec{\mathbf{r}} = \left[r_{\text{cav}}\cos(\phi), r_{\text{cav}}\sin(\phi), z\right],\ z = \Re\left(z_k - z_{k-1}\right) + z_{k-1},\ z_k = \frac{Hk}{n_z} + z_{\text{bottom}},\ \phi = 2\pi\Re \tag{4.20}$$

The direction of a ray emitted from the cavity walls is obtained by assuming gray and diffuse surfaces:

$$\hat{\mathbf{u}} = \hat{\mathbf{u}}_{\text{n}} + \hat{\mathbf{u}}_{\text{t}},\ \hat{\mathbf{u}}_{\text{n}} = \hat{\mathbf{n}}\cos(\theta),\ \hat{\mathbf{u}}_{\text{t}} = \sin(\theta)\left[\hat{\mathbf{t}}_1\cos(\psi) + \hat{\mathbf{t}}_2\sin(\psi)\right],\ \theta = \sin^{-1}(\sqrt{\Re}),\ \psi = 2\pi\Re \tag{4.21}$$

where $\hat{\mathbf{n}}$, $\hat{\mathbf{t}}_1$, and $\hat{\mathbf{t}}_2$ are the normal and tangential vectors of the surface at the emission point. With the ray origin and direction defined, the rays are traced to the nearest

intersection point with the aperture or the cavity walls. For analysis at the intersection point, a random number is generated. If it is less than the absorptivity of the surface, the ray is absorbed, the location of absorption is recorded, and a new ray is launched. Otherwise the ray is reflected and the direction of a diffusely reflected ray is determined using Eq. (4.21). Ray tracing continues until the ray is absorbed or exits the reactor through the aperture. Once all rays from the aperture and cavity walls have been traced, the net heat flux to each surface is given by:

$$q''_{\text{rad},i} = \frac{\left(N_{\text{abs},i} - N_{\text{em},i}\right) q_{\text{ray}}}{A_i} \tag{4.22}$$

As an alternative method for determining the net heat flux at the reactor cavity wall due to the solar source and radiative exchange within the cavity, the net radiation method is applied. The set of equations for the net heat flux from each surface is given by [48]:

$$\frac{q''_{\text{rad},i}}{\varepsilon_i} - \sum_{j=1}^{N} \left(\frac{1}{\varepsilon_j} - 1 \right) F_{i-j} q''_{\text{rad},j} + H_{\text{o},i} = \sigma T_i^4 - \sum_{j=1}^{N} F_{i-j} \sigma T_j^4 \tag{4.23}$$

where $H_{\text{o},i}$ is the incident flux due to the solar source on the surface and $F_{i\text{-}j}$ is the view factor from surface i to surface j [48]. The incident flux is determined using Monte Carlo ray-tracing prior to the start of the simulation. The resulting matrix of equations is solved using Gauss–Jordan elimination with scaled partial pivoting [65].

The radiation simulation, whether by Monte Carlo or the net radiation method, is executed on a structured, axisymmetric mesh with 10 radial and 25 axial elements. The cavity wall temperature is passed from Fluent to the radiation subroutine via a user defined function (UDF). Since the numerical mesh used in the radiation simulations is

coarser than the mesh used for the CFD computations, temperatures averaged over multiple CFD cells contained in radiation cells are used in the radiation simulations.

The net heat flux data for the top, bottom, and cylinder surfaces are returned to Fluent by the user defined function for use as boundary conditions on the cavity wall.

4.7 Results

The baseline simulation parameters used in this study are shown in Table 4.3. These parameters are used unless otherwise specified.

Table 4.3: Baseline simulation parameters in the steady state analysis

Parameter	Symbol	Value
Total number of rays	N_{total}	10,000,000
Inlet temperature (K)	T_{in}	300
Inlet velocity (m s^{-1})	$u_{z,\text{in}}$	0.01
Outer wall heat flux	q''_{wall}	0

Figure 4.2 shows the pressure drop through the reaction zone, which is related to the amount of pumping work needed to push the flowing gases through the packed bed. The pressure varies in the *z* direction only. As the cavity radius increases, the annular area of the reaction zone decreases and the pressure drop through the reaction zone increases. As the cavity length-to-radius ratio increases, the reaction zone becomes longer and the pressure drop through the reaction zone also increases. To reduce the energy requirements for the process, the pressure drop across the bed should be minimized. A cavity with a small radius and small length-to-radius ratio minimizes the pressure drop.

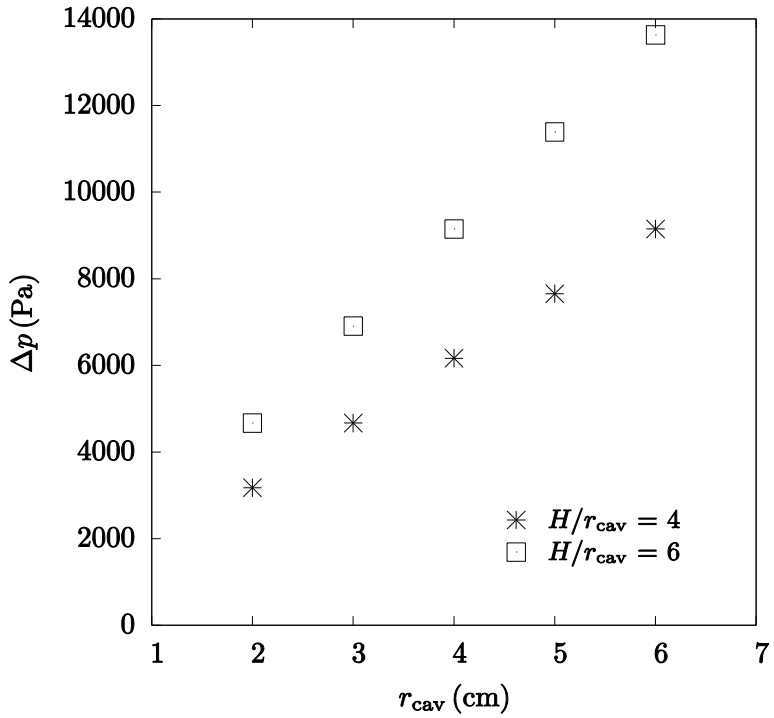

Figure 4.2: Pressure drop through reaction zone

The area-averaged axial temperature increase from the inlet to the outlet of the reaction zone is plotted in Fig. 4.3. Area-averaged temperature is defined as $T_{av} = \frac{1}{A}\sum_{i=1}^{n} T_i A_i$ where A_i is the area of a cell surface facet. The effect of the cavity radius on temperature drop does not have a clear upward or downward trend. There is a minimum value at r_{cav} = 3 cm. For the adiabatic wall boundary condition, the difference between values for cases of different cavity radii is less than 40 K and the difference between values for cases of different length-to-radius ratios is between 10 and 50 K. A shorter cavity reduces the temperature difference slightly. Adding heat loss of 200 W to the outer wall reduces the temperature by about 200 K compared to values for the adiabatic-wall case.

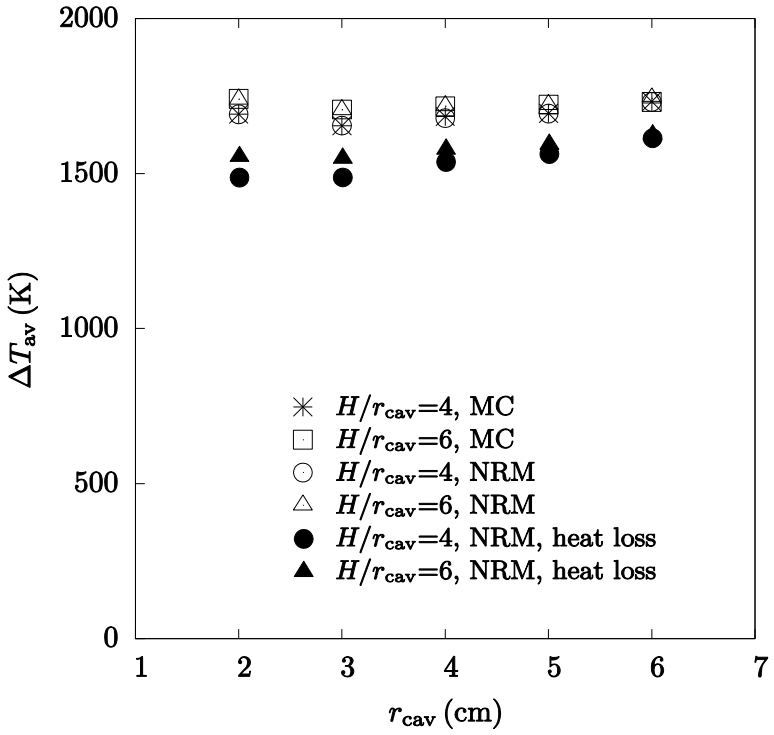

Figure 4.3: Area-averaged axial temperature increase through reaction zone

Figure 4.4 shows the area-averaged radial temperature drop across the reaction zone. Increasing r_{cav} from 2 cm to 6 cm reduces ΔT_{av} due to the corresponding reduction in bed thickness. Higher length-to-radius ratios lower radial temperature drops across the reaction zone by about 3–30 K, but increasing the cavity radius has a stronger effect on the temperature gradients. Adding heat loss of 200 W to the outer wall roughly doubles the temperature drop. This temperature drop should be minimized in order to achieve an even reaction rate throughout the reaction zone.

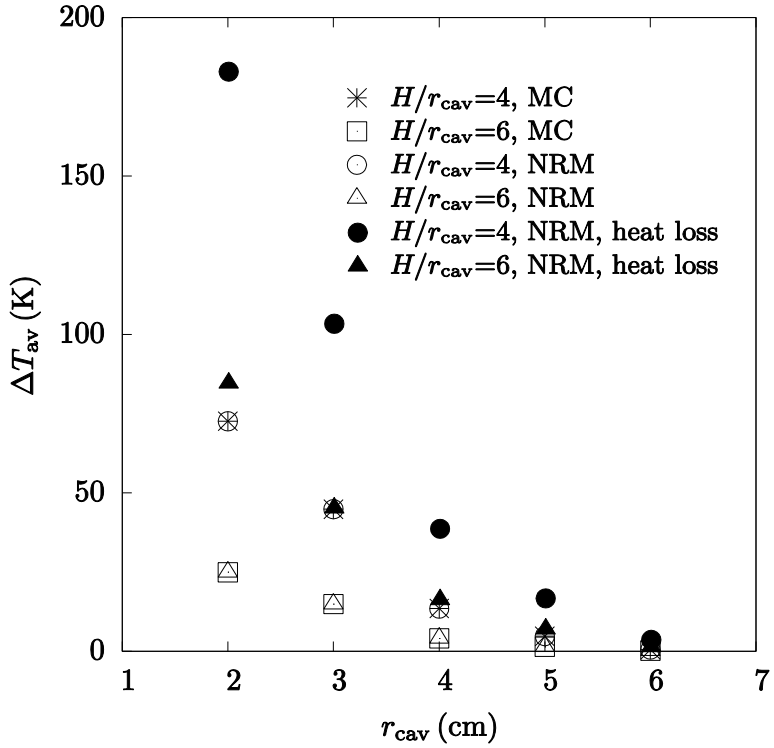

Figure 4.4: Area-averaged radial temperature drop across reaction zone

Area-averaged radial temperature drops across the cavity wall are displayed in Fig. 4.5. In all cases the values of the temperature drop are less than 1.5 K due to the high thermal conductivity of silicon carbide. However, increasing the cavity radius and length-to-radius ratio while holding the reaction zone volume constant further reduces the temperature drop. Heat losses through the outer wall also reduce the temperature drop slightly. This temperature drop should be minimized to reduce thermal stresses in the cavity wall during reactor operation.

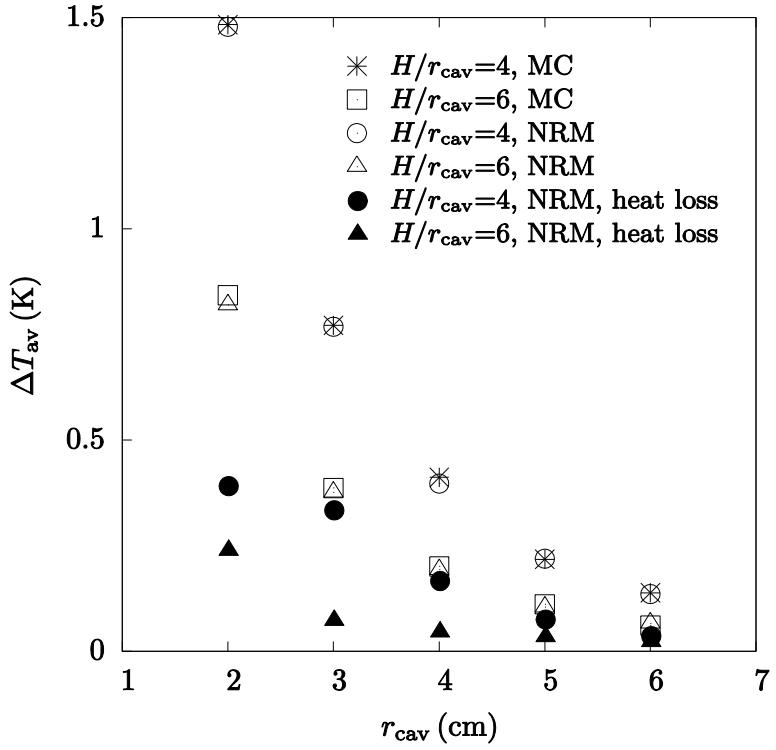

Figure 4.5: Area-averaged radial temperature drop across cavity wall

Figure 4.6 shows the total heat transferred to the reaction zone under steady state operation. Ideally, the reaction zone would receive enough energy such that the reaction rate would not become heat transfer limited, so high rates of heat transfer are desired. The heat rate is highest for r_{cav} = 3 cm when the reaction zone volume and solar concentration ratio are fixed. This is due to competing view factor trends from the cylindrical wall to the aperture and from the top wall to the aperture. As the cavity radius and length-to-radius ratio increase, the view factor from the cylindrical wall to the aperture also increases, but the view factor from the top wall to the aperture decreases. The total heat transfer to the reaction zone increases by about 200 W when heat loss is added to the

outer wall. However, this increase will not contribute to increased solar-to-chemical conversion efficiency as the increase is offset by the 200 W loss through the outer wall.

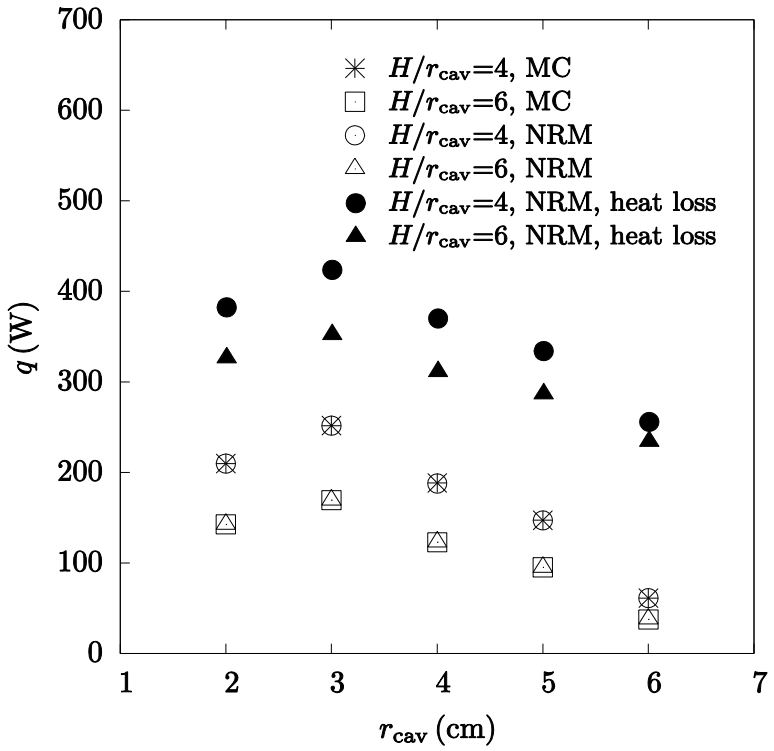

Figure 4.6: Heat transfer rate to reaction zone

Since reaction (1b) becomes thermodynamically favorable above 1150 K at atmospheric pressure, it is important that as much of the reaction zone as possible exceeds this temperature to avoid areas of unreacted particles. In all cases, the reaction zone reaches 1150 K within 5 mm of the inlet. This means that between 95% and 98.5% of the total reaction zone volume is usable for the calcination reaction, with the larger values occurring in the longer reaction zones.

Figure 4.7 shows a comparison of the cavity wall heat flux values between those computed with the Monte Carlo and net radiation methods for the same temperature

distribution. The heat flux from the Monte Carlo calculation with 10 million rays varies by a large amount about values obtained with the net radiation method at some locations in the cavity. Increasing the number of rays to 100 million reduces this variation; however, the computational time increase by doing so is quite large. The relative difference[4] in temperature drop across the reaction zone (Fig. 4.4) is between 0.02% and 0.38% and the relative difference in heat rate to the reaction zone (Fig. 4.6) is between 0.02% and 0.34% for all cases. The net radiation method reaches convergence in 2/3rds the time required for the Monte Carlo method with 10 million rays. From both computational time and accuracy standpoints, the net radiation method is preferred.

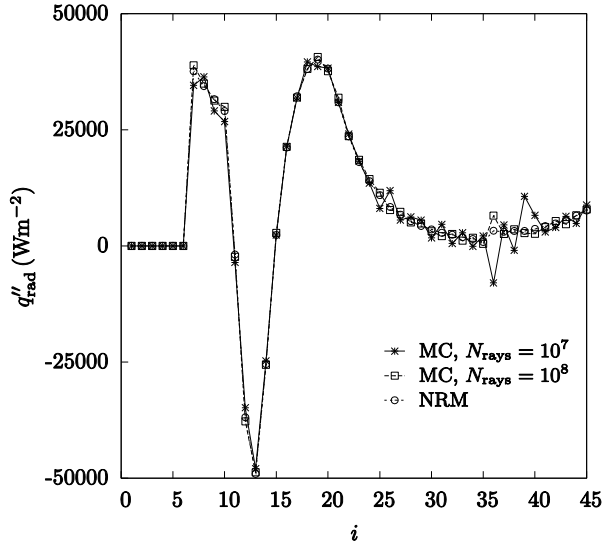

Figure 4.7: Comparison of axial heat flux profiles obtained with Monte Carlo and net radiation methods

[4] Defined as $x = \frac{|x_{\mathrm{MC}} - x_{\mathrm{NRM}}|}{x_{\mathrm{NRM}}}$ for a generic quantity x.

4.8 Summary

The reactor concept selected in Chapter 3 is evaluated using a numerical heat and mass transfer model. The Monte Carlo ray-tracing and net radiation methods are employed to solve for radiative exchange in the inner cavity, coupled with a computational fluid dynamics analysis to solve the mass, momentum, and energy equations in the concentric reaction zone that is modeled as a gas-saturated porous medium consisting of optically large semitransparent particles. The net radiation method reaches convergence 1.5 times faster than the Monte Carlo ray-tracing method and provides smoother radiative flux distribution.

The cavity radius is varied from 2 to 6 cm and the length-to-radius ratio is varied from 4 to 6 to study their effects on pressure drop, temperature distribution, and heat transfer in the reactor. Increasing the cavity radius and length-to-radius ratio decreases the radial temperature gradients across the cavity wall and reaction zone, reducing thermal stresses in the cavity wall and helping ensure uniform reaction rates. However, increasing the cavity radius also results in increased pressure drop through the reaction zone and reduced heat transfer to the reaction zone. Because of these competing effects, a moderate cavity radius of 3 or 4 cm is likely to be the most beneficial choice for this type of reactor.

CHAPTER 5: REACTOR ENGINEERING DESIGN[5]

5.1 Design Specifications

With the effect of cavity dimensions established, the next step in designing the reactor is to outline the design specifications, including materials, insulation thicknesses, and overall part dimensions. These specifications are then used as a starting point for the detailed mechanical design. Based on the modeling results obtained in Chapter 4, the radius and height of the reactor cavity were selected to be 4 cm and 16 cm, respectively. This choice strikes a balance between increasing heat transfer to the reaction zone and the desire for a uniform temperature throughout the reaction zone.

The initial insulation thickness was selected using a one-dimensional heat loss analysis. Figure 5.1 shows results from these calculations. In Fig. 5.1a, the insulation thickness was varied to study its effect on the conduction losses in the radial direction. Initially the losses are over 40% of the total solar energy entering the reactor, but they begin to level off between 10 and 20 cm of insulation thickness. In Fig. 5.1b, the cavity temperature was varied to determine the sensitivity of the heat loss calculation to this variable. The reradiation through the reactor aperture is most sensitive to the cavity wall

[5] Material in this chapter has been published in L. Reich, L. Melmoth, R. Gresham, T. Simon, and W. Lipinski. Design of a Solar Thermochemical Reactor for Calcium Oxide Based Carbon Dioxide Capture. *Proceedings of the ASME 2015 Power & Energy Conference*, San Diego, CA, June 28-July 2, 2015 [78].

temperature, as the losses depend on cavity temperature to the fourth power. The other losses increase linearly with temperature.

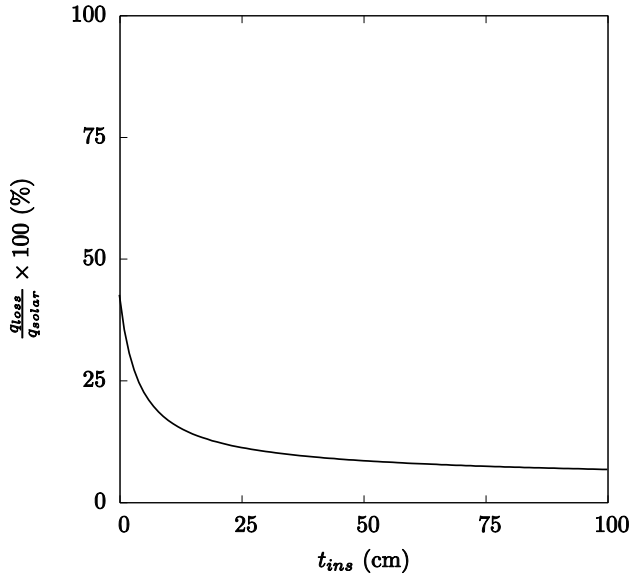

Figure 5.1a: Effect of insulation thickness on conduction heat losses in the radial direction. The cavity wall temperature is 1500 K.

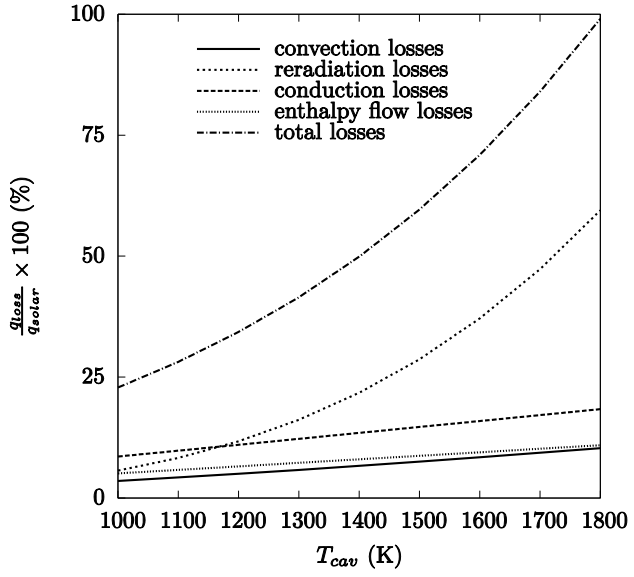

Figure 5.1b: Sensitivity of heat loss calculations to the cavity wall temperature. The insulation thickness is 10 cm.

The reactor materials were selected based on their ability to withstand the expected temperatures and chemical environment in the reactor. These materials are primarily ceramics, although steel alloys can be used for lower temperature areas of the reactor, such as the outer shell. Initially, alumina was considered for the cavity material, the thinking being that its semitransparent nature would improve heat transfer to the reaction zone. However, the thermal conductivity of the alumina is low, about 30 W m^{-1} K^{-1}, and the transmittance of alumina decreases strongly with thickness, from 0.5 at 0.13 mm to 0.3 at 0.25 mm [66,67]. For structural stability, the thickness of the cavity wall would be at least 5 to 10 mm thick, so the transmittance at this thickness is likely to be negligible, and the low thermal conductivity presents the risk of fracture due to high temperature gradients in the cavity wall. For these reasons, silicon carbide was selected as the cavity material in place of alumina. The nominal part dimensions and proposed materials are shown in Table 5.1.

Table 5.1: Reactor design specifications

Part	Material	Inner Diameter	Outer Diameter	Height
Cavity	SiC	8 cm	9 cm	16 cm
Annular wall	SiC	11.3 cm	12.3 cm	17 cm
Top Shell	Stainless steel	-	53 cm	0.5 cm
Bottom Shell	Stainless steel	26 cm	53 cm	0.5 cm
Mid Shell	Stainless steel	32 cm	33 cm	37 cm
Aperture	Alumina/silica board	3.57 cm	32 cm	15 cm
Distributor plate/cavity bottom	SiC	3.57 cm	13 cm	0.5 cm
Particle screen	Inconel	-	12 cm	
Outer Insulation	Alumina/silica board	12.3 cm	32 cm	27 cm
Top Insulation	Alumina/silica board	-	8 cm	10 cm
Gaskets	Mica	33 cm	52.5 cm	
Reaction zone	$CaCO_3$/CaO particles	-	-	-
Gas inlet tubes	Inconel			
Bolts	Steel			

5.2 Design Refinement

5.2.1 Mechanical Design[6]

The engineering design of the reactor was conducted using the concept of Fig. 3.1c and the design specifications outlined in Table 5.1 as a starting point. This discussion on design analysis is separated into four primary systems: gas distribution, irradiance capture, reaction cavity, and structural support.

The gas distribution system consists of two manifolds to allow gas to flow through the reaction zone. Gaskets are used to prevent the gas from entering other areas of the reactor. The manifold is designed to produce a uniform, laminar flow into the reaction zone while having a single inlet and outlet for ease of experimental setup. The manifold ring radius, cross sectional radius, number of center pipes, and radius of the center pipes were varied to find a combination that achieved the design goals. Geometrical constraints and Reynolds number within the pipes were determined. The manifold design is shown in Fig. 5.2. The manifold ring radius is 140 mm, the cross-sectional radius is 17.5 mm, the number of center pipes is 6, and the radius of the center pipes is 15 mm. The manifold material is Inconel 625.

---

[6] Section 5.2.1 describes work completed by Luke Melmoth, an undergraduate student at The Australian National University, as part of an honors thesis under the supervision of Robert Gresham [79]. A summary is presented here in order to form a cohesive narrative describing the reactor design process.

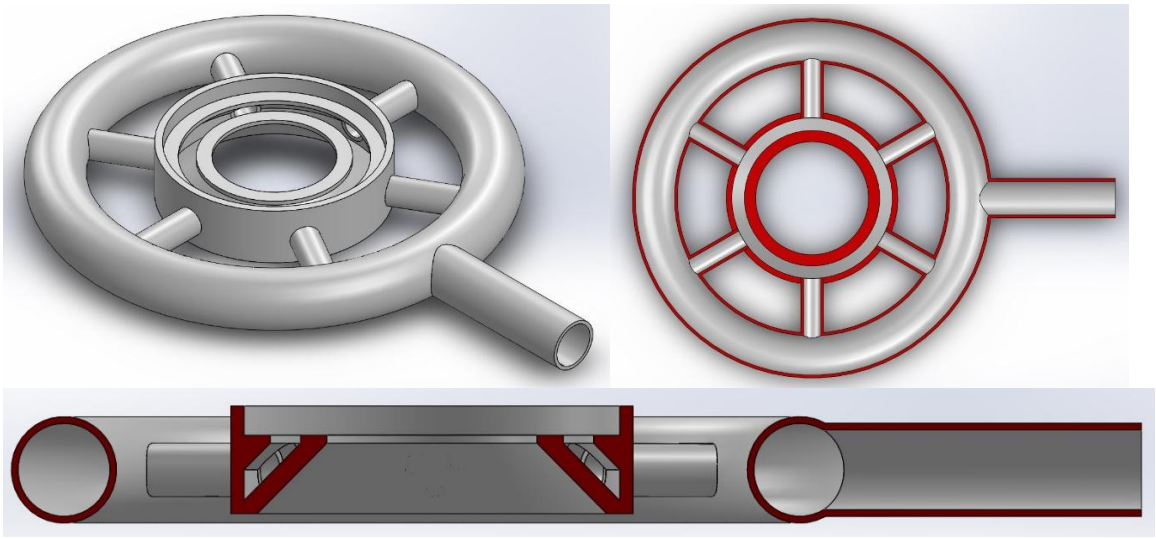

Figure 5.2: Bottom manifold design (top–left: trimetric view; top–right: top cross–section view; bottom: side cross-section view)

Recesses for eight gaskets of two sizes are designed for placement between the manifold, distributor plate, and reaction zone walls to form a gas tight seal during reactor operation while allowing the reactor to be disassembled between experiments. The gaskets are constructed of Fiberfrax DS [68], a ceramic paper that can be easily cut into the correct shape, can withstand the expected temperatures in the reactor, and can be replaced between experiments, as necessary.

The irradiance capture system consists of the reactor aperture cone, two distributor plates, and the cavity wall. The aperture cone angle must be equal to or greater than the cone angle of the incident solar irradiation in order to allow the irradiation to enter the reactor cavity without impinging on aperture parts. The aperture cone consists of a single part made of Inconel 625. The two distributor plates form the top and bottom walls of the reactor cavity and facilitate gas flow from the plenum into the reaction zone. The bottom

distributor plate has a hole to allow solar radiation to enter the reactor cavity. The desired input power of 1 kW and solar concentration of 1000 result in an aperture diameter of 35.7 mm. The bottom distributor plate is shown in Fig. 5.3. The bevel provides a surface for the gasket, cavity wall, and manifold to be located, and provides structural support. The number and size of the outer holes are constrained by the laminar flow requirement. At least 50% of the circumferential material must remain for structural stability. This results in a distributor plate with 19 holes, each 9 mm in diameter. The cylindrical cavity wall absorbs the solar irradiation and conducts it to the reacting bed of particles. The reactor cavity dimensions, the radius of 40 mm, and the height of 160 mm, were chosen based on the predicted pressure drop, temperature distribution, heat transfer rate to the reaction zone, and receiver absorption efficiency as described in Chapter 4. The distributor plates and cavity wall are made of CoorsTek Ultra SiC [66].

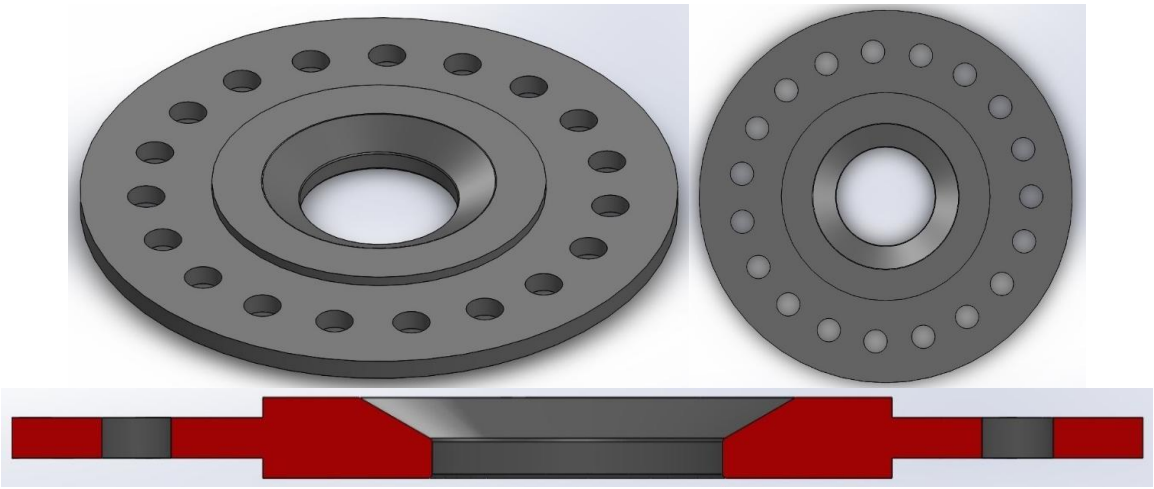

Figure 5.3: Bottom distributor plate design (top–left: isometric view, top–right: top view, bottom: side cross-section view)

The reaction cavity system consists of the cavity wall, reaction zone outer wall, distributor plates, and a particle screen. The cylindrical outer wall forms the final component of the reaction zone, sealing the reacting particles from the outer components of the reactor. It is made of CoorsTek Ultra SiC. The particle screen, shown in Fig. 5.4, is a fine Inconel wire mesh which acts as a barrier to stop fine particles from falling through the distributor plate. The particle screen was added rather than reducing the size and increasing the number of distributor plate holes, reducing manufacturing complexity. The diameter of the screen holes is 0.5 mm.

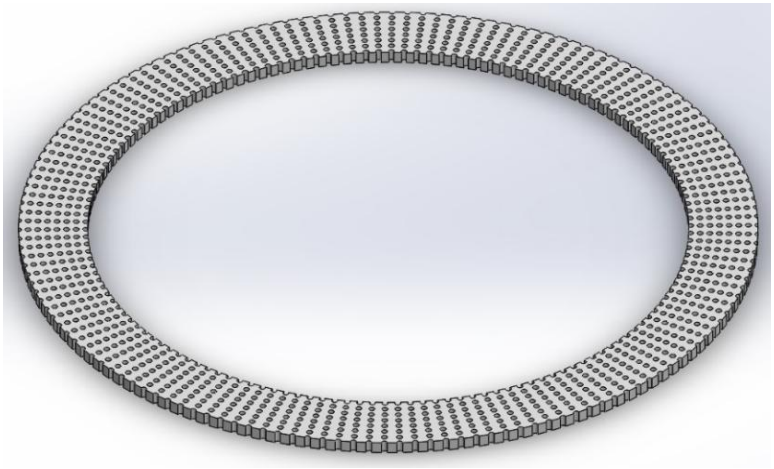

Figure 5.4: Particle screen design

The structural support system includes the reactor shell, insulation, clamp mounts, springs, bolts, and nuts. These components provide the necessary force to create a gas tight seal around the reaction zone and manifolds. The reactor shell is of 304 stainless steel, offering strength at low cost. The clamp mounts fit on the top and bottom of the manifolds and are held secured by the bolts, Belleville springs, and nuts. The clamping assembly along with the reaction cavity and manifold system is shown in Fig. 5.5.

Each system design was evaluated with ANSYS to determine deformation, mechanical loading, and possible failure conditions due to temperature loading, thermal expansion, and physical forces. The reactor component designs offer a minimum safety factor of 5.

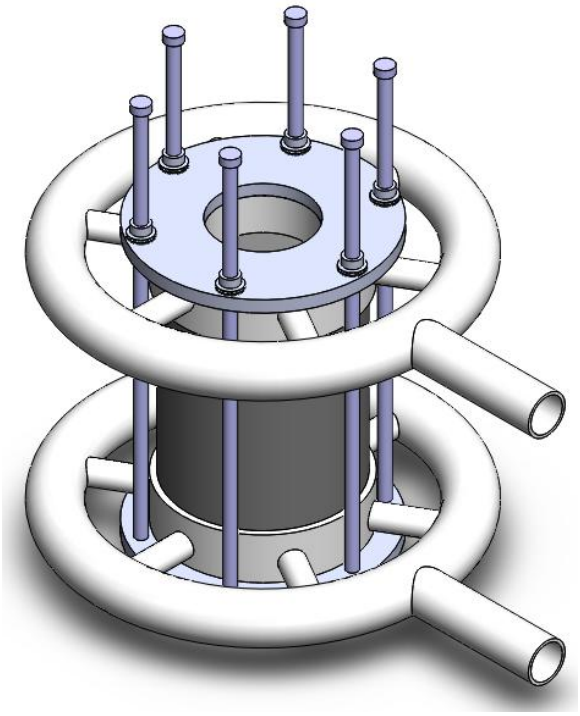

Figure 5.5: Clamping assembly

The overall design history of the reactor is shown in Fig. 5.6. The first iteration added a gas inlet manifold allowing only one gas connection each. With the second iteration the thickness of the cavity wall and reaction zone outer wall were increased to improve mechanical strength, the gas manifold was moved to inside the insulation in order to reduce losses from the hot exit gases, and the manifold design was changed from a square cross section to a round one to improve fluid flow and manufacturability. The third iteration increased the insulation thickness to reduce heat losses and changed the

insulation material from a solid piece to a loose fill and made minor changes to the aperture hole.

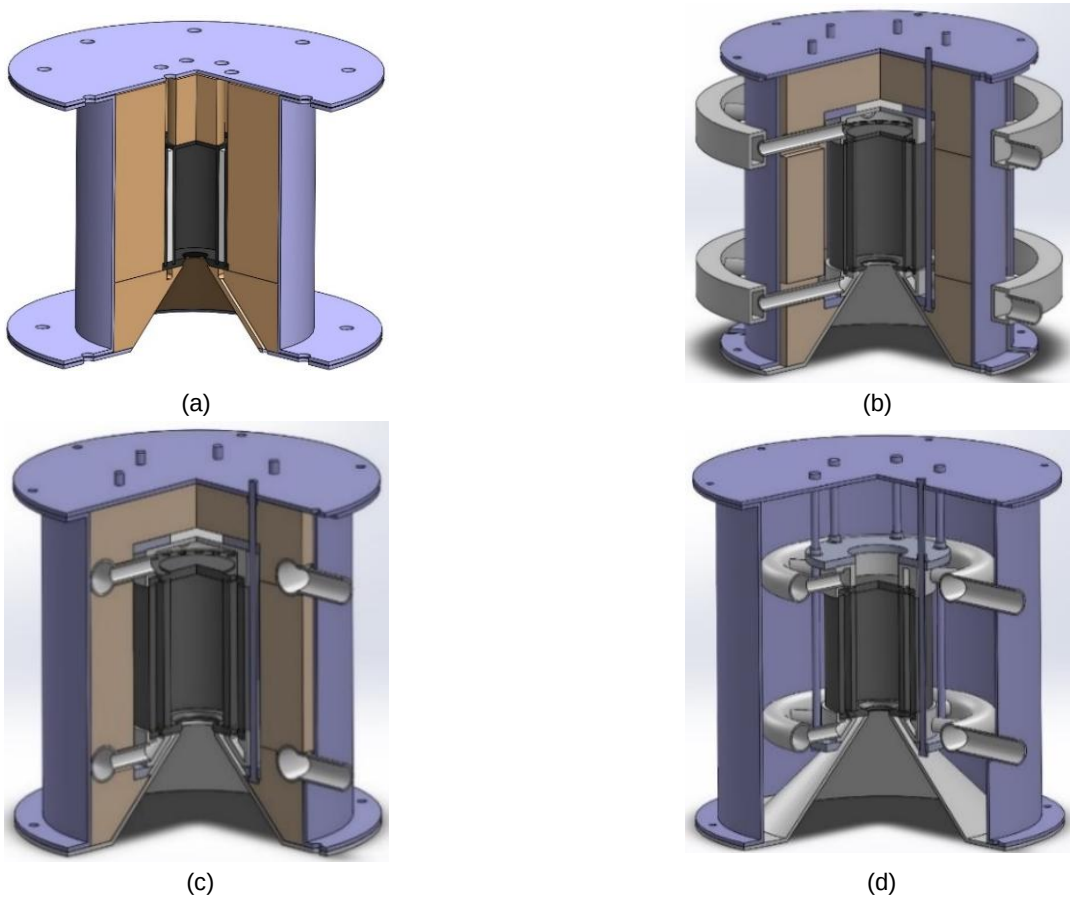

Figure 5.6: Reactor design history: (a) Initial design, (b) 1st iteration, (c) 2nd iteration, (d) 3rd iteration

5.2.2 Thermal Design

The reactor design is evaluated using the thermal transport model developed in Chapter 4. The model domain consists of half of the reactor, taking advantage of symmetry about the axis of the manifold inlet and outlet. For evaluation of thermal transport, each part of the reactor is assumed to be in perfect contact with adjoining parts. The exterior of the reactor is assumed to be in contact with air at 300 K. A heat transfer

coefficient of 5 W m^{-2} K^{-1} is applied. Carbon dioxide sweep gas enters the reactor at 300 K with a mass flow rate of 2.8 x 10^{-4} kg s^{-1}, the flow rate expected assuming the calcium carbonate particles in the reactor are completely calcined in 30 minutes. The particles in the reactor have a uniform diameter of 1 mm and the volume fraction of particles in the packed bed is 0.6. The incident 1 kW radiative flux enters the reactor aperture with a cone angle of 45°, equal to that of typical solar concentrators as well as the solar simulator where the reactor will be tested [51]. Chemical reactions and body forces such as gravity are not included in the model. The goal of the modeling is to determine the maximum temperature limits of the reactor in order to identify potential structural problems. Neglecting the endothermic calcination reaction produces the most conservative temperature estimate. During testing, the temperatures in the reactor will be controlled by tuning the incident solar radiation and amount of preheating of the incoming gases.

The steady state conservation equations were solved for each iteration of the reactor design in order to identify locations where temperatures approach the melting temperature of the employed materials and where high-temperature gradients lead to high thermal stresses. Temperature profiles for two different design iterations are shown in Fig. 5.7. Figure 5.7(a) shows the results for the initial materials selection as described in section 5.2.1. This result shows areas near the aperture and at the top of the reaction zone where the Inconel and stainless steel parts reach temperatures close to their melting points (roughly 1560 K and 1660 K, respectively). In Fig. 5.7(b), the material for the top

and bottom distributor plates and the reaction zone outer wall was changed to mullite in order to better insulate the metal from the high temperatures in the reaction zone. The temperatures of the metal parts are lower by about 100 K compared to those in Fig. 5.7(a), but there are still high-temperature gradients in the Inconel near the aperture. Thus, a two-part aperture with the area closest to the aperture made of high density alumina was added to the final design, and the temperature profile is shown in Fig. 5.7(c). The temperature at the aperture has been reduced by about 100 K without affecting the reaction zone temperatures significantly.

There are three main heat loss categories: convection and conduction losses through the outer walls (29–33% of the total predicted losses), reradiation losses through the aperture (56–60% of the total predicted losses), and losses due to gas flows through the reaction zone (10–11% of the total predicted losses). The addition of chemistry is likely to alter these proportions, which is explored in Chapter 6.

5.3 Final Design

The final design of the reactor is shown in Fig. 5.8. It incorporates all of the design features described previously. The reactor materials and material properties are shown in Table 5.2. Perhaps the most important feature of this reactor design is its flexibility. Each part is designed to be easily removable, allowing for changes in materials or dimensions to meet other temperature or chemical reaction requirements. This will allow the reactor to be used to study a wide range of chemical reactions, not just the CaO carbonation–

calcination cycle described in this work. The distributor plate and particle screen could also be modified to allow the reactor to be run in a fluidized bed mode.

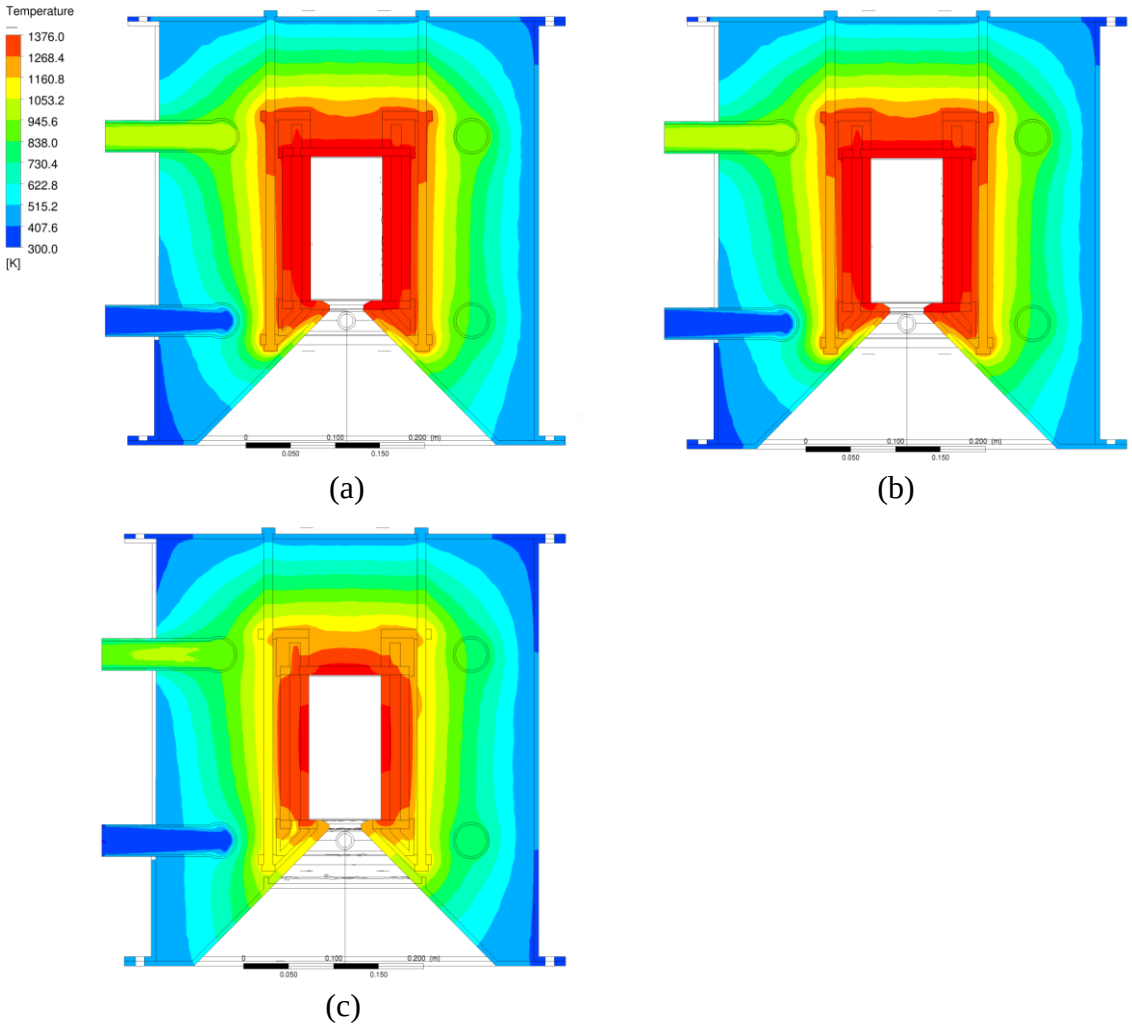

Figure 5.7: Temperature profiles for three reactor design iterations

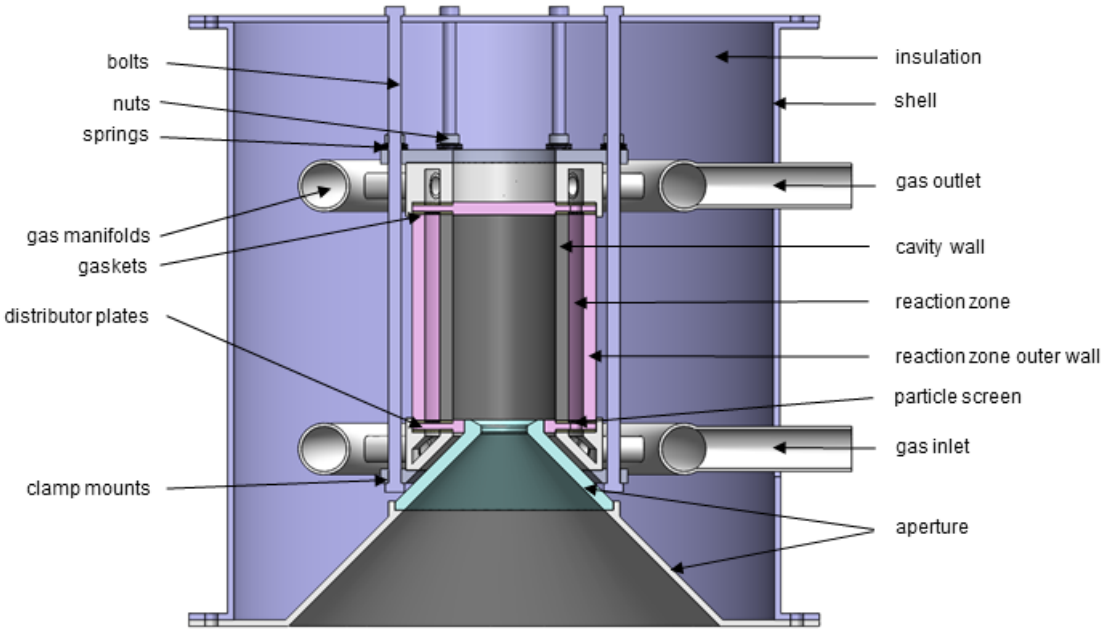

Figure 5.8: Final reactor design

The modular reactor design allows for easy assembly and disassembly between experiments, facilitating morphological and composition characterization of the reacting particles at various stages of cycling. The assembly steps are shown in Fig. 5.9. First, the bottom distributor plate is taken and the particle screen and gaskets are located. Second, the bottom distributor plate is placed into the bottom manifold and the cavity wall and reaction zone outer wall are located and placed on top. The reaction zone can then be filled with particles. Third, the top distributor plate, gaskets, and particle screen are placed on top of the walls. Fourth, the top manifold is placed on top of the distributor plate. Fifth, the clamping components are placed on top and bottom of the reaction zone assembly and tightened. Sixth, the top shell is mounted. Seventh, the assembly is placed inside the outer shell and the top and outer shells are screwed together. The loose

insulation is poured into the reactor. Finally, the two aperture parts are attached to the bottom of the reactor, completing the assembly.

Table 5.2: Reactor materials and material properties

Material	Parts	Color in Fig. 5.8	Density ($kg\ m^{-3}$)	Specific Heat ($J\ kg^{-1}\ K^{-1}$)	Thermal Conductivity ($W\ m^{-1}\ K^{-1}$)	Ref.
Ultra SiC	cavity wall	dark gray	3150	800	125	[66]
Mullite	distributor plates, reaction zone outer wall	pink	2800	950	3.5	[66]
Alumina AD-998	top part of aperture	light blue	3920	880	30	[66]
SS 304	shell, bolts, nuts, springs, clamp mounts	purple	8000	500	21.5	[69]
Inconel 625	bottom part of aperture, manifolds, particle screen	light gray	8440	410	9.8	[70]
Fiberfrax bulk fiber	insulation	–	160	1130	0.14	[71]
Fiberfrax DS paper	gaskets	white	160	–	0.08	[68]

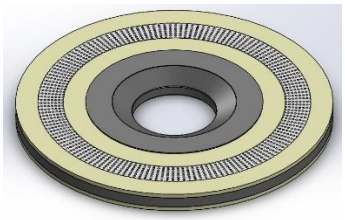

Step 1

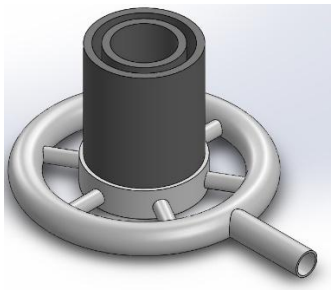

Step 2

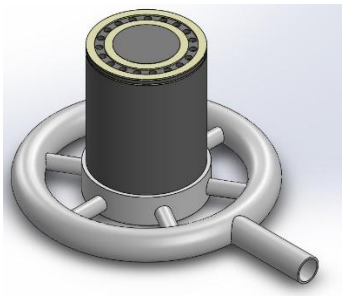

Step 3

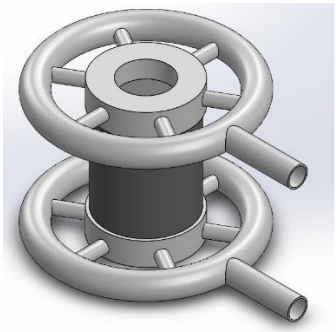

Step 4

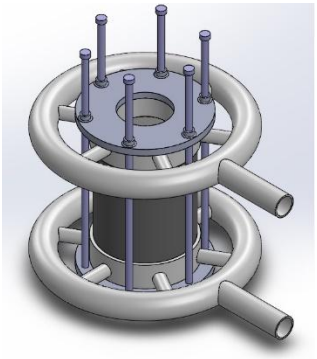

Step 5

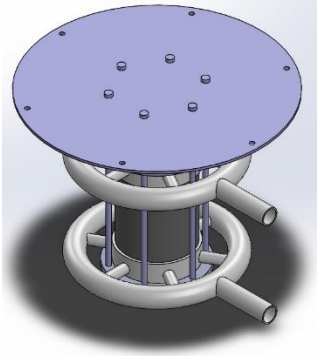

Step 6

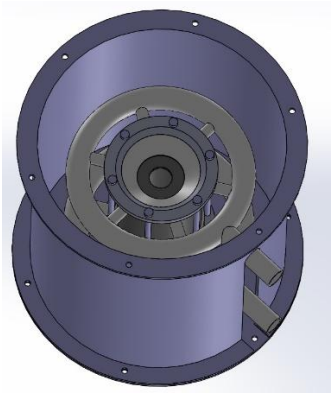

Step 7

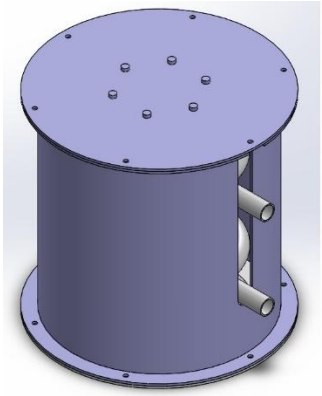

Step 8

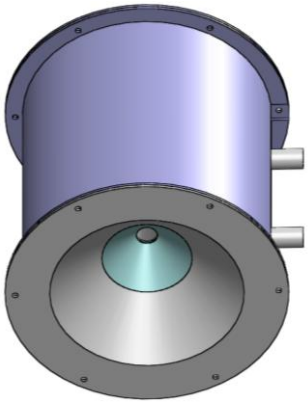

Figure 5.9: Reactor assembly steps

CHAPTER 6: TRANSIENT HEAT AND MASS TRANSFER MODEL WITH CHEMISTRY

6.1 Introduction

An important performance parameter for the reactor is the solar-to-chemical conversion efficiency. With a higher efficiency, more CaO can be regenerated for a given solar energy input and reaction time, improving the overall CO_2 capture rate of the process. Because the solar-to-chemical conversion efficiency depends on the chemical kinetics, which are inherently transient, the steady state model described in Chapter 4 is insufficient to predict the efficiency of the reactor. This chapter presents a transient model of the reactor during the calcination step.

6.2 Governing Equations

The unsteady continuity equation for the gas phase has the form:

$$\frac{\partial \rho}{\partial t} + \nabla \cdot (\rho \vec{\mathbf{v}}) = \bar{M}_{\mathrm{CO_2}} \dot{r} \tag{6.1}$$

where ρ is density of the gas mixture, t is time, $\vec{\mathbf{v}}$ is velocity, $\bar{M}$ is molar mass, and $\dot{r}$ is the molar volumetric rate of generation of CO_2 by the calcination reaction.

The unsteady momentum equation is:

$$\frac{\partial}{\partial t}(\rho \vec{\mathbf{v}}) + \nabla \cdot \left(\rho \vec{\mathbf{v}} \vec{\mathbf{v}}\right) = -\nabla p + \nabla \cdot \left(\bar{\bar{\boldsymbol{\tau}}}\right) + \vec{\mathbf{S}} \tag{6.2}$$

where p is pressure, $\bar{\bar{\boldsymbol{\tau}}}$ is the shear stress tensor, and $\vec{\mathbf{S}} = -\left(\frac{\mu}{K}\vec{\mathbf{v}} + \frac{1}{2}C_{\mathrm{f}}\rho\left|\vec{\mathbf{v}}\right|\vec{\mathbf{v}}\right)$ accounts for the pore-level viscous (Darcy) and inertial losses in the packed bed of reacting particles.

As in Chapter 4, the packed bed is modeled as an isotropic porous media. K is the permeability and C_f is the Forchheimer coefficient of the porous zone. The Ergun equation is used to derive K and C_f for the packed bed, resulting in $\frac{1}{K} = \frac{150 f_{v,s}^2}{D_p^2 (1 - f_{v,s})^3}$ and $C_f = \frac{3.5 f_{v,s}}{D_p (1 - f_{v,s})^3}$ [53]. In these calculations, the bed is assumed to be isotropic with $D_p = 1\text{x}10^{-3}$ m and $f_{v,s} = 0.6$, a typical value for a randomly packed bed of uniform spheres.

The unsteady energy equation assuming thermal equilibrium between the fluid and solid phases in the reaction zone is:

$$\frac{\partial}{\partial t}\left[(1 - f_{v,s})\rho_f E_f + f_{v,s}\rho_s h_s\right] + \nabla \cdot \left[\vec{\mathbf{v}}\left(\rho_f E_f + p\right)\right] = -\nabla \cdot \vec{\mathbf{q}}_{rad}^{"} + \nabla \cdot (k_{eff} \bar{\nabla} T) + S \qquad (6.3)$$

where $E_f = h_f - \frac{p}{\rho_f} + \frac{v^2}{2}$ is the total fluid energy, h_s is the solid enthalpy, $\vec{\mathbf{q}}_{\mathbf{rad}}^{"}$ is the internal radiative heat flux in the bed, k_{eff} is the effective thermal conductivity, determined using the homogenous model, $k_{eff} = (1 - f_{v,s})k_f + f_{v,s}k_s$, T is temperature, h is enthalpy, and the subscripts f and s indicate fluid and solid, respectively. A source term that accounts for the heat of chemical reaction is defined as $S = -\Delta\bar{h}_T^0 \dot{r}$ where $\Delta\bar{h}_T^0$ is the molar reaction enthalpy at the reaction temperature. The Rosseland diffusion approximation is used to calculate the internal radiative heat flux, $\vec{\mathbf{q}}_{rad}^{"} = -k_{rad}\nabla T$, where $k_{rad} = \frac{16 n^2 \sigma T^3}{3\beta}$, n is the real part of the refractive index of the host medium, and β is the

extinction coefficient. The extinction coefficient is calculated using the method of geometric optics [48]. In the solid regions of the reactor, the energy equation reduces to $\frac{\partial}{\partial t}(\rho h) = k\nabla^2 T$.

As mentioned in Chapter 1, a wide variety of reaction rate expressions for calcination appear in the literature. Since the gas atmosphere and particle size used in [25] are similar to those considered for the reactor, the rate expression from that paper is chosen for the simulation:

$$\frac{\mathrm{d}X}{\mathrm{d}t} = k(1-X)^{2/3}\,\frac{p_{\mathrm{CO_2}} - p_{\mathrm{eq,CO_2}}}{RT} \tag{6.4}$$

where $k = k_0 \exp\left(\frac{-E_\mathrm{a}}{RT}\right)$ is the rate constant, $k_0 = 2.38$ x 10^4 $\mathrm{m^3\ mol^{-1}\ s^{-1}}$ is the pre-exponential factor, $E_\mathrm{a} = 150$ kJ $\mathrm{mol^{-1}}$ is the activation energy, $X = 1 - \frac{n_{\mathrm{CaCO_3}}(t)}{n_{\mathrm{CaCO_3},0}}$ is the reaction extent, $n_{\mathrm{CaCO_3},0}$ is the initial number of moles of $CaCO_3$, $p_{\mathrm{CO_2}}$ is the actual partial pressure of CO_2, $p_{\mathrm{eq,CO_2}} = 4.137\mathrm{x}10^{12} \exp\left(\frac{-20474}{T}\right)$ is the equilibrium partial pressure of CO_2, and T is temperature. The molar volumetric reaction rate is related to the conversion rate by $\dot{r} = \frac{\mathrm{d}X}{\mathrm{d}t}\frac{n_0}{V_\mathrm{s}}$, where V_s is the solid volume.

6.3 Boundary and Initial Conditions

The model geometry consists of half of the reactor as shown in Fig. 5.8, recognizing the plane of symmetry through the axis of the inlet and outlet. The boundary conditions are

- At the inlet:

Eq. (6.1) $$\rho_{\mathrm{f}}\left(\vec{\mathbf{v}}\cdot\hat{\mathbf{n}}\right)\Big|_{\mathrm{inlet}} = \rho_{\mathrm{f}} u_{\mathrm{in}} \tag{6.5}$$

Eq. (6.3) $$T\big|_{\mathrm{inlet}} = T_{\mathrm{in}} \tag{6.6}$$

- At the outlet:

Eq. (6.2) $$p\big|_{\mathrm{outlet}} = 0 \tag{6.7}$$

- At the plane of symmetry:

Eq. (6.2) $$\vec{\mathbf{v}}\cdot\hat{\mathbf{n}} = 0 \tag{6.8}$$

Eq. (6.3) $$\nabla T\cdot\hat{\mathbf{n}} = 0 \tag{6.9}$$

- At the inner cavity wall:

Eq. (6.3) $$-k\nabla T\cdot\hat{\mathbf{n}} = q''_{\mathrm{rad}} \tag{6.10}$$

- At the outer surfaces of the reactor:

Eq. (6.3) $$-k\nabla T\cdot\hat{\mathbf{n}} = h(T - T_{\infty}) \tag{6.11}$$

- At interfaces between materials:

Eq. (6.3) $$-k_1\nabla T_1\cdot\hat{\mathbf{n}}_1 = -k_2\nabla T_2\cdot\hat{\mathbf{n}}_2 \tag{6.12}$$

The locations of the above boundary conditions are shown in Fig. 6.1. The initial conditions and parameters used to evaluate the boundary conditions used in the simulation are shown in Table 6.1.

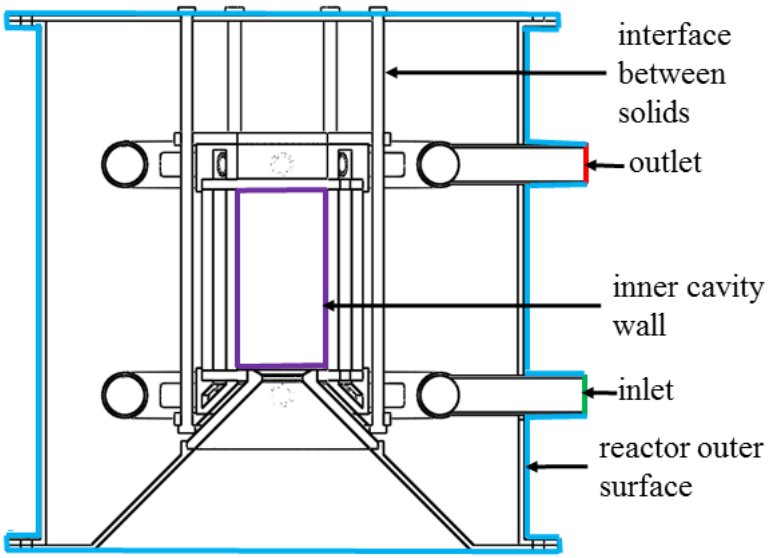

Figure 6.1: Boundary condition locations (green: inlet, red: outlet, purple: inner cavity wall, blue: reactor outer surfaces, black: interface between solids)

Table 6.1: Initial conditions and parameters used to evaluate boundary conditions

Parameter	Symbol	Value
Inlet temperature (K)	T_{in}	300
Inlet velocity (m s^{-1})	u_{in}	0.22
Initial temperature (K)	$T(t=0)$	650
Initial velocity (m s^{-1})	$u(t=0)$	0.22
Convection coefficient (W m^{-2} K^{-1})	h	5
Ambient temperature (K)	T_{∞}	300

6.4 Thermophysical Properties

The thermophysical properties of the porous solid are calculated by mass fraction weighted averaging of the individual properties of each constituent. The general form of this averaging is $L = \sum_i y_i L_i$ where L is some property and y_i is the mass fraction of species i. For example, the density of the solid is $\rho_s = \sum_i y_i \rho_i$ where ρ_i is the density of species i.

The thermophysical properties of the carbon dioxide are the same as in Table 4.2. The thermophysical properties of the reactor materials are shown in Table 6.2.

Table 6.2: Thermophysical properties of materials in the transient analysis

Material	Property[7]			
	ρ (kg m^{-3})	k (W m^{-1} K^{-1})	c_p (J kg^{-1} K^{-1})	Ref.
Alumina	3920	30	880	[66]
Mullite	2800	3.5	950	[66]
Silicon Carbide	3150	150	800	[66]
SS 304	8000	21.5	500	[69]
Inconel	8440	9.8	410	[72]
Fiberfrax Insulation	160	0.14	1130	[68]
Calcium Oxide	3350	0.8	$50.42+4.18\text{x}10^{-3}T-8.5\text{x}10^{5}T^{-2}$	[73–75]
Calcium Carbonate	2170	0.6	$104.52+2.192\text{x}10^{-2}T-2.59\text{x}10^{6}T^{-2}$	[73–75]

[7] At 25°C

6.5 Numerical Solution

The finite volume technique as implemented in ANSYS Fluent 15.0 is used to solve the conservation equations on a mesh with approximately 3,300,000 cells. Time discretization is first-order implicit. The continuity equation is solved using the projection method and the SIMPLE segregated pressure–velocity coupling algorithm [62,63]. The momentum and energy equations are solved with a second-order upwind scheme. Gradients are evaluated using a least squares cell-based discretization scheme. The radiative flux profile on the cavity wall, q''_{rad}, is modeled using the net radiation method (NRM) described in Section 4.6. The computational time to obtain the results shown in section 6.6 was approximately 2 months running a serial calculation using 32 GB of memory.

The mass and energy source terms, reaction rate, and thermophysical properties of the reacting particles are calculated using user defined functions (UDFs) and stored as user defined memory (UDM). User defined memory saves selected data generated by the UDF for future access and analysis. The sequence for calling UDFs in the Fluent solver process is shown in Fig. 6.2.

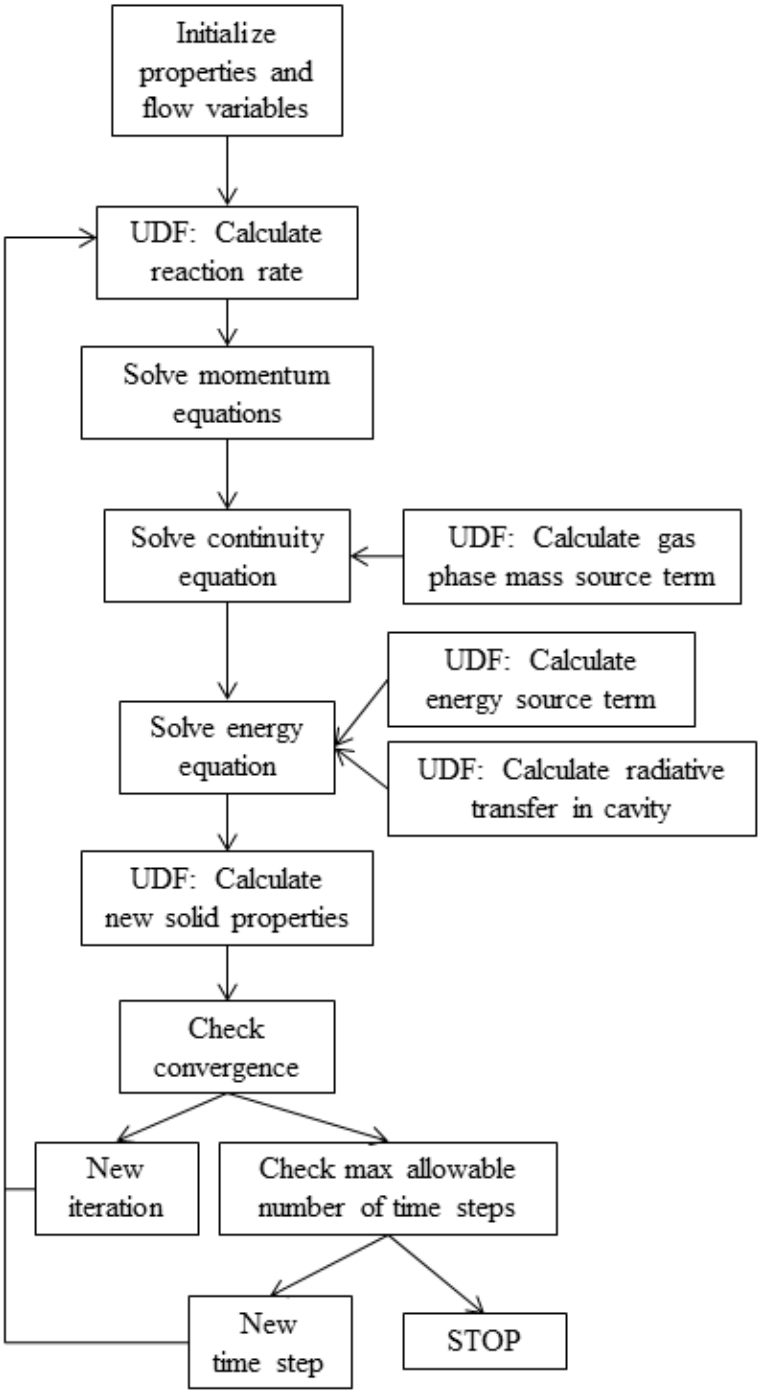

Figure 6.2: User defined function (UDF) calling sequence in Fluent (modified from [76])

A limitation of the Fluent software is the inability to access UDM in the UDF that defines specific heat. Since the specific heat of the solid is a function of the composition, which is tracked with the reaction extent UDM, a workaround is required. The solid specific heat only appears in the h_s term of Eq. (6.3), which Fluent calculates as $h_s = \int_{T_{ref}}^{T} c_{p,s} dT$. The specific heat of the solid in the Fluent solver is artificially set equal to unity, reducing h_s to (T-T_{ref}) in Eq. (6.3). A modified density term is then introduced that includes the real solid specific heat, $\rho_s^* = \frac{\rho_s \int_{T_{ref}}^{T} c_{p,s} dT}{(T - T_{ref})}$. When both ρ_s^* and the artificial h_s are substituted into Eq. (6.3), the original form of the equation is retained.

6.6 Results

Temperature profiles in the reactor at various instances in time are shown in Fig. 6.3. The temperature at the top of the cavity increases at the highest rate, and the areas of highest temperature spread outward and downward as time progresses. The maximum temperature in the reactor at t=300 min is 1260 K.

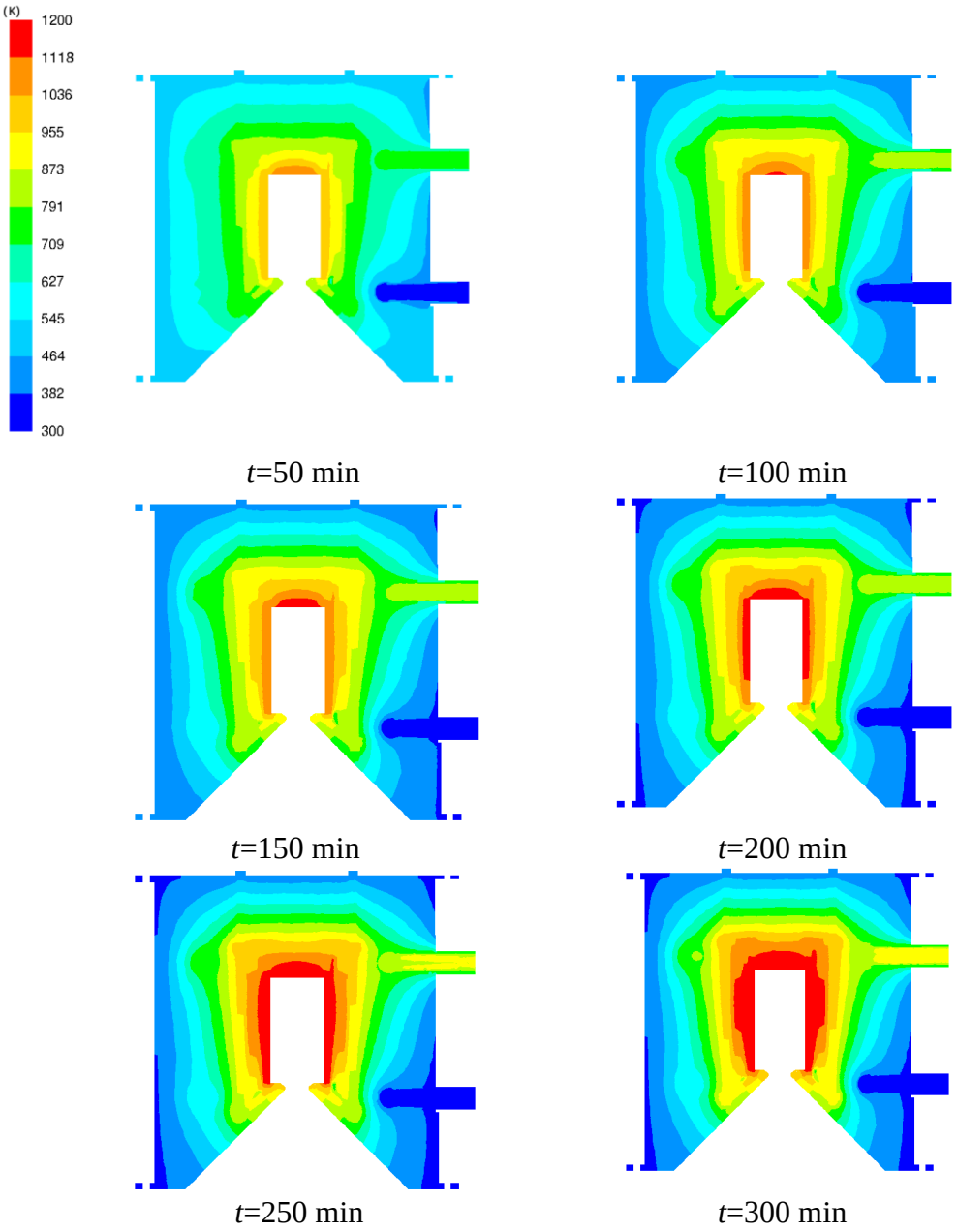

Figure 6.3: Transient temperature profiles in the reactor

Profiles of reaction extent at various instances in time are displayed in Fig. 6.4. At *t*=50 min, the reaction is just starting near the inner walls on the upper half of the reaction zone. The reaction front proceeds outward and downward concomitant with the

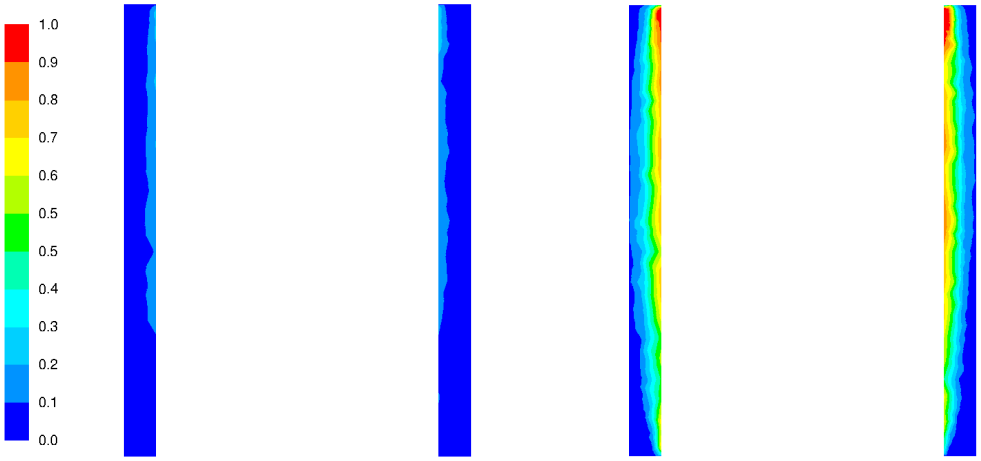

t=50 min *t*=100 min

t=150 min *t*=200 min

t=250 min *t*=300 min

Figure 6.4: Transient reaction extent profiles in the reaction zone

increasing temperature in the reaction zone. Between *t*=200 min and *t*=300 min there is very little change as the reaction approaches completion. There is a small amount of asymmetry due to the presence of the gas inlet to the bottom right of the reaction zone.

The overall reaction extent, $X = 1 - \frac{n_{CaCO_3}(t)}{n_{0,CaCO_3}}$, as a function of time is shown in Fig. 6.5. The reaction begins at around *t*=20 min. After an initial startup period lasting until *t*=40 min, the reaction extent increases linearly for the majority of the calcination step. When the reaction extent approaches 0.87 around *t*=200 min, the (1-*X*) term in Eq. (6.4) begins to dominate, slowing the reaction rate and causing the curve to flatten, consistent with the results of Fig. 6.4.

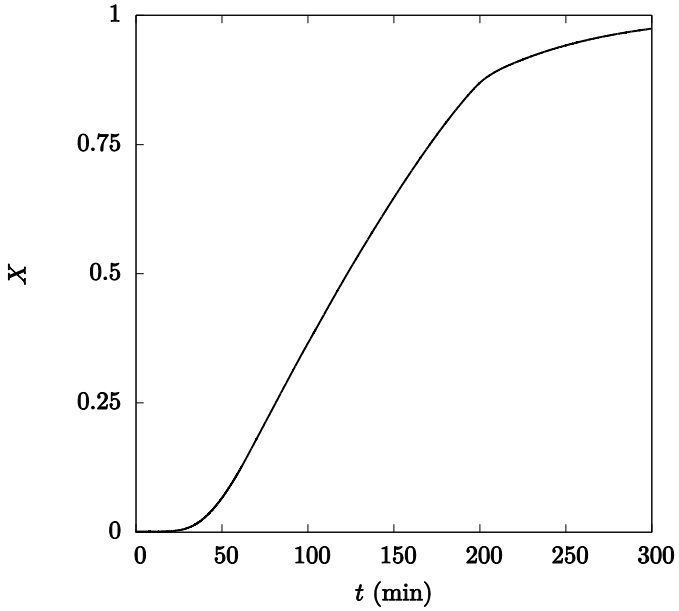

Figure 6.5: Reaction extent, X, as a function of time

The volume-averaged reaction zone temperature is shown in Fig. 6.6. Initially, the temperature increases at a higher rate because the calcination reaction has not started,

meaning the energy sink term in Eq. (6.3) is zero. Once the reaction starts, the rate of increase slows and becomes roughly linear after 40 min. After the reaction begins to taper off at t=200 min, the rate of temperature increase accelerates once again as the reactor comes to a steady state temperature.

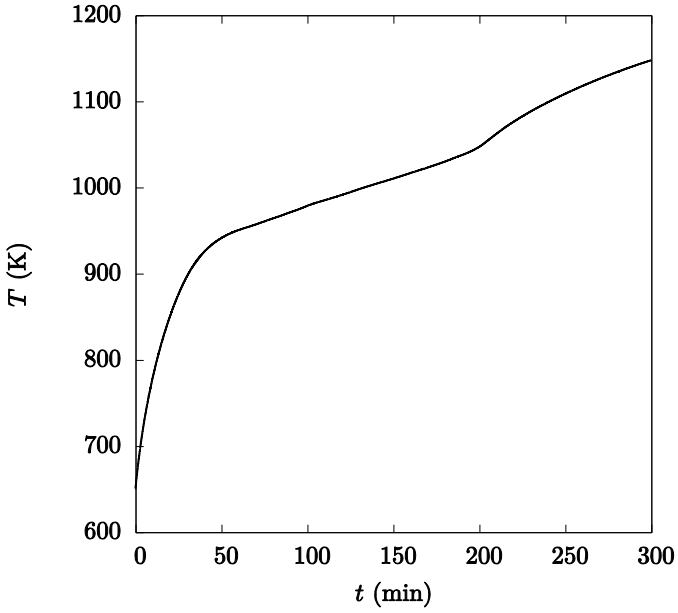

Figure 6.6: Volume averaged reaction zone temperature

The solar-to-chemical conversion efficiency, defined as $\eta(t) = \frac{\dot{r} V_{\text{rxn}} \Delta h^0_{\text{calc},298K}}{q_{\text{solar}}}$, is shown in Fig. 6.7. The efficiency reaches a maximum value of 26% at t=149 min. The average solar-to-chemical conversion efficiency, $\bar{\eta} = \frac{(n_{\text{CaCO}_3,t_1} - n_{\text{CaCO}_3,t_2}) \Delta h^0_{\text{calc},298K}}{(t_2 - t_1) q_{\text{solar}}}$, is 6% for t_1=25 min and t_2=200 min. As shown in the thermodynamic analysis of Chapter 2, the addition of gas heat recovery to the process can reduce the heat requirements

significantly. If the energy required to heat the gases is included in the efficiency, $\eta^*(t) = \frac{\dot{r}V_{\text{rxn}}\Delta h^0_{\text{calc},298K} + \dot{m}_{\text{g}} c_{\text{p,g}} \Delta T}{q_{\text{solar}}}$, then the maximum value is 35%.

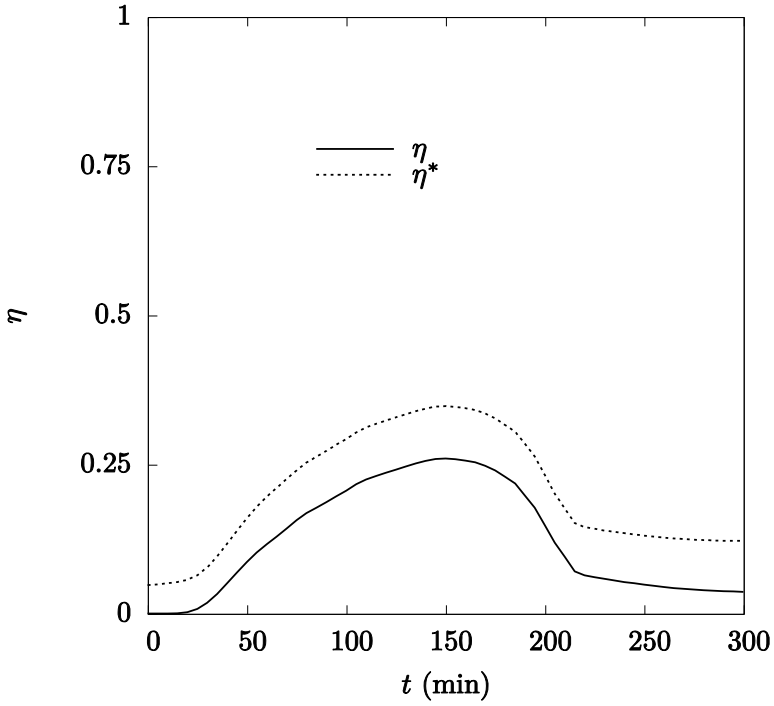

Figure 6.7: Solar-to-chemical conversion efficiency

The heat balance in the reactor is shown in Fig. 6.8. The largest source of heat loss is conduction through the reactor walls, followed by reactor heating. The conduction losses are high initially due to the constant temperature initial condition. As seen in Fig. 6.3, the outer walls of the reactor actually cool down as the simulation progresses, and the conduction heat loss reaches a steady state value near 300 W. Both reradiation and flow losses remain below 100 W for the entire simulation. Thus, it would seem that increasing the insulation thickness may be the simplest way of increasing the reactor efficiency. However, since the reactor is intended to cycle between low and high temperature steps,

care must be taken to ensure that the thermal inertia of the reactor is not so high as to make the cooling or heating time between steps unreasonable. Improving heat transfer within the reaction zone could also increase the efficiency by making the reaction zone temperature more uniform. As shown in Figs. 6.3 and 6.4, the areas of high temperature spread outward and downward as the reaction progresses, so increasing this rate of spread may help increase the reaction rate. This could possibly be accomplished by adding fins to the cavity wall or placing nonreacting high thermal conductivity particles in the reaction zone. Gas preheating or recycling could also be employed to increase the efficiency, as shown in Fig. 6.7.

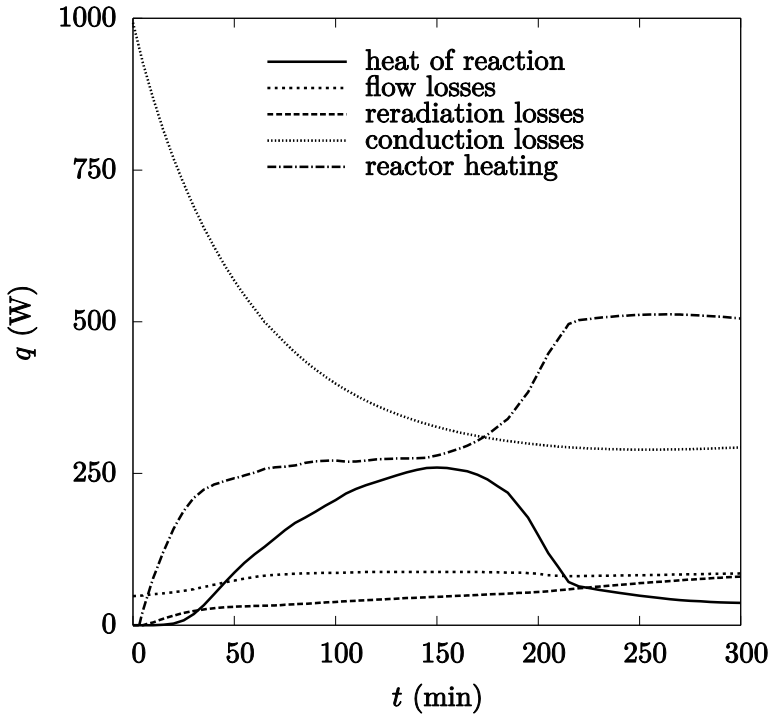

Figure 6.8: Heat balance in the reactor

6.7 Summary

The reactor design described in Chapter 5 is evaluated using a numerical heat and mass transfer model. The net radiation method is employed to solve for radiative exchange in the inner cavity with a user defined function, coupled with a computational fluid dynamics analysis to solve the mass, momentum, and energy equations in the reactor. User defined functions are also employed to calculate the calcination reaction rate, mass and energy source terms, and thermophysical properties of the reacting particles. The maximum solar-to-chemical efficiency achieved is 26%, and the maximum efficiency including gas heating is 35%. The average efficiency is 6%. The reaction front spreads outward and downward, following the increasing temperatures in the reactor. The primary source of heat loss is conduction through the reactor walls, which could be reduced by increasing the insulation thickness. However, the benefit of increased insulation thickness must be weighed against the increased cycling time. Additional design improvements such as adding fins to improve heat transfer in the reaction zone may also help improve the efficiency.

CHAPTER 7: SUMMARY AND OUTLOOK

7.1 Summary

A thermodynamic analysis of the CaO–based carbonation–calcination process was conducted to determine the effect of reaction temperature, gas and solid heat recovery, and inlet gas CO_2 concentration on the total solar heat required for the process. The heat requirements to capture atmospheric levels of CO_2 with this process are prohibitively high, over 45 MJ per mole of CO_2 captured with no heat recovery. However, it is well matched to higher CO_2 concentrations such as those found in power plant flue gas, with heat requirements as low as 207 kJ per mole of CO_2 captured with perfect gas and solid heat recovery. While important in the overall energy balance, gas phase heat recovery can be implemented externally to the reactor vessel using commercially available heat exchangers. Solid phase heat recovery is of smaller importance, and its implementation would add considerable complexity to the reactor design.

Several reactor concepts were compared and a single concept was chosen for evaluation using a numerical heat and mass transfer model. The Monte Carlo ray-tracing and net radiation methods were employed to solve for radiative exchange in the inner cavity, coupled with a computational fluid dynamics analysis to solve the mass, momentum, and energy equations in the reaction zone. The cavity radius and length-to-radius ratio were varied to study their effects on pressure drop, temperature distribution, and heat transfer in the reactor. This information was used to select the dimensions of the reactor cavity. From there, the reactor design was refined using mechanical and thermal

analyses to select appropriate dimensions and materials, resulting in a final design that is easy to assemble and flexible enough to be used to study a wide range of thermochemical processes.

The reactor design was evaluated using a transient numerical heat and mass transfer model in order to predict its solar-to-chemical conversion efficiency. The maximum solar-to-chemical efficiency achieved was 26%, and the maximum efficiency including gas heating was 35%. The average efficiency was 6%. The primary source of heat loss was conduction through the reactor walls, which could be reduced by increasing the insulation thickness. However, the benefit of increased insulation thickness should be weighed against the increased cycling time. Additional design improvements such as adding fins to the reaction zone to improve heat transfer or adding gas preheating or recycling could also improve the efficiency.

7.2 Recommendations for Future Work

Further work on the heat and mass transfer model of this reactor should expand the reaction simulation to include the carbonation step, which will allow a one-to-one comparison of the model results to those obtained with the thermodynamic analysis. Several different reaction expressions could be tested to evaluate the sensitivity of the model to the particular expression used. The radiative heat transfer and chemical reaction codes could be parallelized in order to increase the speed of future calculations. Once experimental results are available, the model needs to be validated against them. If

experimental results indicate a need to improve the reactor, the model could then be used to quickly evaluate various ideas without the expense of purchasing and testing each one.

Once the reactor is manufactured, it must be tested and its performance evaluated. In addition to the reactor itself, an experimental platform must be constructed for data collection during tests. The platform must include equipment to measure temperature, gas flow rates, gas composition, and solar power input. A schematic of what the experimental setup might look like is shown in Fig. 7.1.

Each experiment should consist of a number of carbonation and calcination cycles. The history of the particles in the reactor should be tracked to help determine the effect of cycling on each sorbent. There are a number of independent variables that can be changed to create an experimental plan to evaluate the reactor. The independent variables that can be changed are shown in Table 7.1a. Each independent variable is shown with a suggested range of values to investigate. The measured outputs of each experiment are shown in Table 7.1b along with a measurement device or technique that could be used.

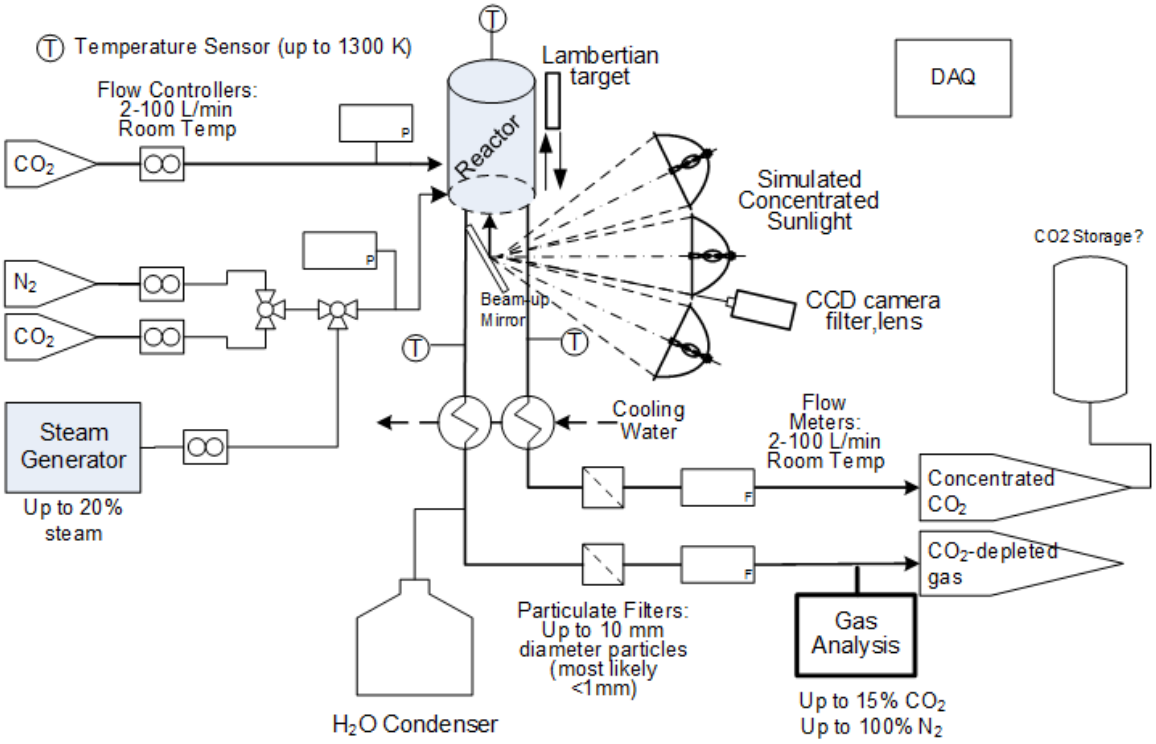

Figure 7.1: Preliminary schematic of experimental setup

Table 7.1a: Independent variables and suggested range of values for experiments

Independent variable	Symbol	Suggested range of values
Calcination temperature	T_{calc}	800–1100°C
Carbonation temperature	T_{carb}	25–600°C
Carbonation atmosphere		0.05–15% CO_2, 0-20% steam, 65–99.95% N_2
Calcination atmosphere		100% CO_2 or 100% inert gas (N_2 or Ar)
Particle size	d_p	$1x10^{-6}$–$10x10^{-3}$ m
Sorbent source		Alfa Aesar CaO powder, GLC Envirocal 345, GLC Envirocal 346d, other limestone sources, possibly other carbonates (e.g. Na_2CO_3, $MgCO_3$)
Number of cycles		1–50

Table 7.1b: Measured outputs and suggested measurement techniques

Measured outputs	Symbol	Measuring device or technique
Temperatures	T	Type K or S thermocouples
Inlet and outlet gas flow rate	$\dot{m}$	Mass flow controller or flow meter
Inlet and outlet gas composition		Gas chromatograph, mass spectrometer, or Raman laser gas analyzer
Solar power input	$\dot{Q}_{\text{solar}}$	CCD camera and Lambertian target
Particle morphology (after run): size distribution, grain size, composition		SEM, X-ray diffraction, or computed tomography

The measured outputs can be used to calculate three metrics to evaluate the reactor's performance: overall CO_2 capture rate, molar specific heat required to capture CO_2, and solar to chemical conversion efficiency. The overall CO_2 capture rate, $\dot{n}_{\text{CO}_2,\text{ captured}}$, accounts for the absorption rate of the carbonation reaction as well as the release rate of the calcination reaction. It is defined as:

$$\dot{n}_{\text{CO}_2,\text{ captured}} = \frac{\dot{n}_{\text{calc}}\dot{n}_{\text{carb}}}{\dot{n}_{\text{calc}} + \dot{n}_{\text{carb}}} \tag{7.1}$$

where $\dot{n}_{\text{calc}}$ is the rate of release of CO_2 in the calcination step and $\dot{n}_{\text{carb}}$ is the rate of absorption of CO_2 in the carbonation step. Both terms are obtained using the gas flow rate and composition measurements at the inlet and outlet for the two process steps. The molar heat required to capture CO_2 is defined as:

$$\overline{Q} = \frac{\dot{Q}_{solar}}{\dot{n}_{\text{CO}_2,\text{ captured}}} \tag{7.2}$$

and can be compared to the results from the thermodynamic analysis to quantify how close the reactor comes to being ideal. The solar to chemical conversion efficiency

describes how well the reactor delivers solar energy to the calcination reaction. It is defined as:

$$\eta = \frac{\dot{n}_{\text{calc}} \Delta H^{0}_{\text{calc}}}{\dot{Q}_{\text{solar}}} \tag{7.3}$$

The measured outputs can be used to construct maps of the reactor performance metrics as a function of the independent variables. These maps can then be used to identify regions of maximum CO_2 capture rate and efficiency as well as pinpoint areas where the reactor design could be improved by comparing the needed solar energy to the thermodynamic limit. The research-scale reactor can also be used to study other chemical processes, such as CO_2 capture using other carbonates or thermochemical energy storage. Ultimately, the insights gained from the experimental campaign combined with use of the numerical model can be used to develop a scaled-up version of the reactor so it can be demonstrated at an industrial scale.

REFERENCES

[1] U.S. Energy Information Administration, 2009, Emissions of greenhouse gases in the United States 2008.

[2] Anderson, J., Fercusson, M., and Valsecchi, C., 2008, An overview of global greenhouse gas emissions and emissions reduction scenarios for the future, Institute for European Environmental Policy.

[3] U.S. Energy Information Administration, 2011, International Energy Outlook 2011, Washington, D.C.

[4] BP, 2012, BP Statistical Review of World Energy 2012.

[5] Leckel, D., 2009, "Diesel production from Fischer-Tropsch: The past, the present, and new concepts," Energy & Fuels, **23**, pp. 2342–2358.

[6] Metz, B., Davidson, O., de Coninck, H. C., Loos, M., and Meyers, L. A., eds., 2005, IPCC Special Report on Carbon Dioxide Capture and Storage, Cambridge University Press, Cambridge.

[7] Rackley, S. A., 2010, Carbon Capture and Storage, Butterworth-Heinemann/Elsevier, Burlington.

[8] Gupta, H., and Fan, L., 2002, "Carbonation-calcination cycle using high reactivity calcium oxide for carbon dioxide separation from flue gas," Ind. Eng. Chem. Res., **41**, pp. 4035–4042.

[9] Abanades, J. C., Rubin, E. S., and Anthony, E. J., 2004, "Sorbent cost and performance in CO2 capture systems," Ind. Eng. Chem. Res., **43**, pp. 3462–3466.

[10] Steinfeld, A., and Palumbo, R., 2001, "Solar Thermochemical Process Technology," Encyclopedia of Physical Science & Technology, R.A. Meyers, ed., Academic Press, pp. 237–256.

[11] Kodama, T., and Gokon, N., 2007, "Thermochemical cycles for high-temperature solar hydrogen production.," Chem. Rev., **107**, pp. 4048–4077.

[12] Wu, J., and feng Long, X., 2015, "Research progress of solar thermochemical energy storage," Int. J. Energy Res., **39**, pp. 869–888.

[13] Edwards, S. E. B., and Materić, V., 2012, "Calcium looping in solar power generation plants," Sol. Energy, **86**, pp. 2494–2503.

[14] Shimizu, T., Hirama, T., Hosoda, H., Kitano, K., Inagaki, M., and Tejima, K., 1999, "A Twin Fluid-bed Reactor for Removal of CO_2 from Combustion Processes," Chem. Eng. Res. Des., **77**, pp. 62–68.

[15] Rodriguez, N., Alonso, M., Grasa, G., and Abanades, J. C., 2008, "Heat requirements in a calciner of $CaCO_3$ integrated in a CO_2 capture system using CaO," Chem. Eng. J., **138**, pp. 148–154.

[16] Martínez, A., Lara, Y., Lisbona, P., and Romeo, L. M., 2012, "Energy penalty reduction in the calcium looping cycle," Int. J. Greenh. Gas Control, **7**, pp. 74–81.

[17] Nikulshina, V., Hirsch, D., Mazzotti, M., and Steinfeld, a, 2006, "CO_2 capture from air and co-production of H2 via the $Ca(OH)_2$–$CaCO_3$ cycle using concentrated solar power–Thermodynamic analysis," Energy, **31**, pp. 1715–1725.

[18] Nikulshina, V., Galvez, M., and Steinfeld, A., 2007, "Kinetic analysis of the carbonation reactions for the capture of CO_2 from air via the $Ca(OH)_2$–$CaCO_3$–CaO solar thermochemical cycle," Chem. Eng. J., **129**, pp. 75–83.

[19] Borgwardt, R. H., 1985, "Calcination kinetics and surface area of dispersed limestone particles," AIChE J., **31**, pp. 103–111.

[20] Dennis, J. S., and Hayhurst, A. N., 1987, "The effect of CO_2 on the kinetics and extent of calcination of limestone and dolomite particles in fluidized beds," Chem. Eng. Sci., **42**, pp. 2361–2372.

[21] Escardino, a., Garcia-Ten, J., and Feliu, C., 2008, "Kinetic study of calcite particle (powder) thermal decomposition: Part I," J. Eur. Ceram. Soc., **28**, pp. 3011–3020.

[22] Garcia-Labiano, F., Abad, A., de Diego, L. F., Gayan, P., and Adanez, J., 2002, "Calcination of calcium-based sorbents at pressure in a broad range of CO_2 concentrations," **57**, pp. 2381–2393.

[23] Acharya, B., Dutta, A., and Basu, P., 2012, "Circulating-Fluidized-Bed-Based Calcium-Looping Gasifier : Experimental Studies on the Calcination − Carbonation Cycle," Ind. Eng. Chem. Res., **51**, pp. 8652–8660.

[24] Bhatia, S. K., and Perlmutter, D. D., 1983, "Effect of the product layer on the kinetics of the CO_2-lime reaction," AIChE J., **29**, pp. 79–86.

[25] Fang, F., Li, Z., and Cai, N., 2009, "Experiment and Modeling of CO_2 Capture from Flue Gases at High Temperature in a Fluidized Bed Reactor with Ca-Based Sorbents," Energy & Fuels, **23**, pp. 207–216.

[26] Gallagher, P. K., and Johnson, D. W., 1973, "The effects of sample size and heating rate on the kinetics of the thermal decomposition of $CaCO_3$," Thermochim. Acta, **6**, pp. 67–83.

[27] Sun, P., Grace, J. R., Lim, C. J., and Anthony, E. J., 2008, "Determination of intrinsic rate constants of the CaO–CO_2 reaction," Chem. Eng. Sci., **63**, pp. 47–56.

[28] Lee, D., 2004, "An apparent kinetic model for the carbonation of calcium oxide by carbon dioxide," Chem. Eng. J., **100**, pp. 71–77.

[29] Yue, L., and Lipiński, W., 2015, "A numerical model of transient thermal transport phenomena in a high-temperature solid–gas reacting system for CO_2 capture applications," Int. J. Heat Mass Transf., **85**, pp. 1058–1068.

[30] Stendardo, S., and Foscolo, P. U., 2009, "Carbon Dioxide Capture with Dolomite: A Model for Gas-solid Reaction within the Grains of a Particulate Sorbent," Chem. Eng. Sci., **64**, pp. 2343–2352.

[31] Abanades, J. C., Luesma, M., Anthony, E. J., Lu, D. Y., Salvador, C., and Alvarez, D., 2004, "Capture of CO_2 from Combustion Gases in a Fluidized Bed of CaO," AIChE J., **50**, pp. 1614–1622.

[32] Lu, D. Y., Hughes, R. W., and Anthony, E. J., 2008, "Ca-based sorbent looping combustion for CO_2 capture in pilot-scale dual fluidized beds," Fuel Process. Technol., **89**, pp. 1386–1395.

[33] Rodríguez, N., Alonso, M., Abanades, J. C., Charitos, A., Hawthorne, C., Scheffknecht, G., Lu, D. Y., and Anthony, E. J., 2011, "Comparison of experimental results from three dual fluidized bed test facilities capturing CO_2 with CaO," Energy Procedia, **4**, pp. 393–401.

[34] Flamant, G., Hernandez, D., Bonet, C., and Traverse, J., 1980, "Experimental Aspects of the Thermochemical Conversion of Solar Energy," Sol. Energy **24**, pp. 385–395.

[35] Imhof, A., and Mischler, D., 1992, "Experimental Investigation of an Atmospheric-Open Cyclone Solar Reactor for Solid-Gas Thermochemical Reactions," **114**, pp. 171–174.

[36] Meier, A., Bonaldi, E., Cella, G. M., Lipinski, W., Wuillemin, D., and Palumbo, R., 2004, "Design and experimental investigation of a horizontal rotary reactor for the solar thermal production of lime," Energy, **29**, pp. 811–821.

[37] Meier, A., Bonaldi, E., Cella, G. M., and Lipinski, W., 2005, "Multitube Rotary Kiln for the Industrial Solar Production of Lime," J. Sol. Energy Eng., **127**, pp. 386–395.

[38] Nikulshina, V., Gebald, C., and Steinfeld, A., 2009, "CO_2 capture from atmospheric air via consecutive CaO-carbonation and $CaCO_3$-calcination cycles in a fluidized-bed solar reactor," Chem. Eng. J., **146**, pp. 244–248.

[39] Nikulshina, V., and Steinfeld, A., 2009, "CO_2 capture from air via CaO-carbonation using a solar-driven fluidized bed reactor—Effect of temperature and water vapor concentration," Chem. Eng. J., **155**, pp. 867–873.

[40] Lapp, J., Davidson, J. H., and Lipiński, W., 2012, "Efficiency of two-step solar thermochemical non-stoichiometric redox cycles with heat recovery," Energy, **37**, pp. 591–600.

[41] Favre, E., Bounaceur, R., and Roizard, D., 2009, "A hybrid process combining oxygen enriched air combustion and membrane separation for post-combustion carbon dioxide capture," Sep. Purif. Technol., **68**, pp. 30–36.

[42] Kalafati, D. D., 1991, "Diffusion entropy and theoretical work of gas mixture separation at variable concentration," Inzhenerno-fizicheskij Zhurnal, **61**, pp. 598–604.

[43] "NIST Chemistry WebBook, NIST Standard Reference Database Number 69," Natl. Inst. Stand. Technol.

[44] Reich, L., Ebner, P., Yue, L., and Lipinski, W., 2013, Solar Thermochemical CO_2 Capture: Technical Summary to the University of Minnesota Initiative for Renewable Energy and the Environment.

[45] Reich, L., Bader, R., Simon, T., and Lipinski, W., 2015, "Thermal Transport Model of a Packed-Bed Reactor for Solar Thermochemical CO_2 Capture," Spec. Top. Rev. Porous Media, in press.

[46] Reddi Kari, S. B., and Werther, J., 2003, "Gas distributor and plenum design in fluidized beds," Handbook of Fluidization and Fluid-Particle Systems, pp. 155–170.

[47] Paitoonsurikarn, S., Lovegrove, K., Hughes, G., and Pye, J., 2011, "Numerical Investigation of Natural Convection Loss From Cavity Receivers in Solar Dish Applications," J. Sol. Energy Eng., **133**, p. 021004.

[48] Modest, M. F., 2013, Radiative Heat Transfer, Elsevier, San Diego.

[49] Roger, M., Amsbeck, L., Gobereit, B., and Buck, R., 2011, "Face-Down Solid Particle Receiver Using Recirculation," J. Sol. Energy Eng., **133**, p. 031009.

[50] Muhich, C. L., Ehrhart, B. D., Alshankiti, I., Ward, B. J., Musgrave, C. B., and Wiemer, A. W., 2015, "A review and perspective of efficient H_2 generation via solar thermal water splitting," WIREs Energy Environ., doi: 10.1002/wene.174.

[51] Bader, R., Haussener, S., and Lipinski, W., 2014, "Optical Design of Multisource High-Flux Solar Simulators," J. Sol. Energy Eng., **137**, p. 021012.

[52] Hirsch, C., 1988, "The Basic Equations of Fluid Dynamics," Numerical Computation of Internal and External Flows Volume 1: Fundamentals of Numerical Discretization, John Wiley & Sons, Chichester, pp. 8–23.

[53] Ergun, S., 1952, "Fluid flow through packed columns," Chem. Eng. Prog., **48**, pp. 89–94.

[54] Jaeger, H. M., and Nagel, S. R., 1992, "Physics of the Granular State," Science, **255**, pp. 1523–1531.

[55] Hischier, I., Hess, D., Lipiński, W., Modest, M., and Steinfeld, A., 2009, "Heat Transfer Analysis of a Novel Pressurized Air Receiver for Concentrated Solar Power via Combined Cycles," J. Therm. Sci. Eng. Appl., **1**, p. 041002.

[56] Dombrovsky, L. A., and Ballis, D., 2010, Thermal Radiation in Disperse Systems: An Engineering Approach, Begell House, New York.

[57] Bohren, C., and Huffman, D., 1983, Absorption and scattering of light by small particles, Wiley, New York.

[58] 2014, "ANSYS® Academic Research, Release 15.0."

[59] Dombrovsky, L., and Lipiński, W., 2007, "Transient temperature and thermal stress profiles in semi-transparent particles under high-flux irradiation," Int. J. Heat Mass Transf., **50**, pp. 2117–2123.

[60] CoorsTek, 2013, "Reaction Bonded Silicon Carbide SC-RB Material Properties"

[61] Touloukian, Y. S., 1967, "Properties of Silicon Carbide," Thermophysical Properties of High Temperature Solid Materials, pp. 5:119–140.

[62] Chorin, A. J., 1968, "Numerical solution of Navier-Stokes equations," Math. Comput., **22**, pp. 745–762.

[63] Patankar, S. V., and Spalding, D. B., 1972, “A calculation procedure for heat, mass and momentum transfer in three-dimensional parabolic flows,” Int. J. Heat Mass Transf., **15**, pp. 1787–1806.

[64] Siegel, R., and Howell, J., 2002, Thermal Radiation Heat Transfer, Taylor & Francis, New York.

[65] Atkinson, K. E., 1989, An Introduction to Numerical Analysis, New York : Wiley, New York.

[66] CoorsTek, 2015, Ceramic Material Properties.

[67] Touloukian, Y. S., 1967, “Properties of Aluminum Oxide,” Thermophysical Properties of High Temperature Solid Materials.

[68] Unifrax Australia Pty Ltd, 2015, Fiberfrax Paper Product Information Sheet.

[69] ASM Handbook Program, 1990, ASM Handbook, Volume 1: Vol. 1 Properties and Selection: Irons, Steels, and High-Performance Alloys., Materials Park : A S M International, Materials Park.

[70] 2013, Special Metals INCONEL Alloy 625.

[71] Unifrax Australia Pty Ltd, 2015, Fiberfrax Bulk Fibre Product Information Sheet.

[72] “Special Metals INCONEL Alloy 625,” MatWeb Mater. Prop. Data [Online]. Available: http://www.matweb.com/search/datasheettext.aspx?matguid=4a194f59f35a427dbc5009f043349cb5.

[73] Binnewies, M., and Milke, E., 2002, Thermochemical Data of Elements and Compounds, Wiley-VCH, Weinheim.

[74] Touloukian, Y. S., Powell, R. W., Ho, C. Y., and Klemens, P. G., 1970, Thermochemical Properties of Matter, Thermal Conductivity, Nonmetallic Solids, vol. 2, IFI/Plenum, New York.

[75] Oates, J. A., 1998, Lime and Limestone, Chemistry and Technology, Production and Uses, Wiley-VCH, Weinheim.

[76] 2013, ANSYS Fluent UDF Manual.

[77] Matthews, L., and Lipiński, W., 2012, “Thermodynamic Analysis of Solar Thermochemical CO_2 Capture via Carbonation / Calcination Cycle,” Energy, **45**, pp. 900–907.

[78] Reich, L., Melmoth, L., Gresham, R., Simon, T., and Lipinski, W., 2015, “Design of a solar thermochemical reactor for calcium oxide based carbon dioxide

capture," Proceedings of the ASME 2015 Power & Energy Conference, San Diego, p. 49507.

[79] Melmoth, L., 2014, "Designing a Solar Thermochemical Reactor for Carbon Dioxide Capture," honors thesis, The Australian National University.